Journal of Inorganic Biochemistry 259 (2024) 112652

Contents lists available at ScienceDirect

Journal of Inorganic Biochemistry

journal homepage: www.elsevier.com/locate/jinorgbio

White light increases anticancer effectiveness of iridium(III) complexes toward lung cancer A549 cells

Gechang Li [a,1], Jing Chen [a,1], Yufeng Xie [a], Yan Yang [b,*], Yajie Niu [a], Xiaolan Chen [a], Xiandong Zeng [a], Lin Zhou [a], Yunjun Liu [a,*]

[a] School of Pharmacy, Guangdong Pharmaceutical University, Guangzhou 510006, PR China
[b] Department of Pharmacy, Guangdong Second Provincial General Hospital, 510317, PR China

ARTICLE INFO

Keywords:
Iridium(III) complexes
Photodynamic therapy (PDT)
Apoptosis
Autophagy
Ferroptosis

ABSTRACT

Anticancer activity has been extensively studies. In this article, three ligands 2-(6-bromobenzo[d][1,3]dioxol-5-yl)-1H-imidazo[4,5-f][1,10]phenanthroline (BDIP), 2-(7-methoxybenzo[d][1,3]dioxol-5-yl)-1H-imidazo[4,5-f][1,10]phenanthroline (MDIP), 2-(6-nitrobenzo[d][1,3]dioxol-5-yl)-1H-imidazo[4,5-f][1,10]phenanthroline (NDIP) and their iridium(III) complexes: $[Ir(ppy)_2(BDIP)](PF_6)$ (ppy = deprotonated 2-phenylpyridine, 3a), $[Ir(ppy)_2(MDIP)](PF_6)$ (3b) and $[Ir(ppy)_2(NDIP)](PF_6)$ (3c) were synthesized. The cytotoxicity of 3a, 3b, 3c against Huh7, A549, BEL-7402, HepG2, HeLa, and non-cancer NIH3T3 was tested using 3-(4,5-dimethylthiazole-2-yl)-2,5-diphenyl tetrazolium bromide (MTT) method. The results obtained from the MTT test stated clearly that these complexes demonstrated moderate or non-cytotoxicity toward Huh7, BEL-7402, HepG2 and HeLa except A549 cells. To improve the anticancer efficacy, we used white light to irradiate the mixture of cells and complexes for 30 min, the anticancer activity of the complexes was greatly enhanced. Particularly, 3a and 3b exhibited heightened capability to inhibit A549 cells proliferation with IC_{50} (half maximal inhibitory concentration) values of 0.7 ± 0.3 μM and 1.8 ± 0.1 μM, respectively. Cellular uptake has shown that 3a and 3b can be accumulated in the cytoplasm. Wound healing and colony forming showed that 3a and 3b significantly hinder the cell migration and growth in the S phase. The complexes open mitochondrial permeability transition pore (MPTP) channel and cause the decrease of membrane potential, release of cytochrome C, activation of caspase 3, and finally lead to apoptosis. In addition, 3a and 3b cause autophagy, increase the lipid peroxidation and lead to ferroptosis. Also, 3a and 3b increase the expression of calreticulin (CRT), high mobility group box 1 (HMGB1), heat shock protein 70 (HSP70), thereby inducing immunogenic cell death.

1. Introduction

Cancer continues to proliferate and escalate in incidence in the 20st century [1]. Surgical intervention, radiation therapy, and chemotherapy are employed as conventional approaches for cancer treatment. Chemotherapy involves administering cytotoxic drugs that target both resting and dividing cells. The objective of cancer chemotherapy is to impede the multiplication, invasion, metastasis, and fatality caused by cancer cells [2]. Despite the progress made in therapeutic approaches such as targeted therapies that focus on oncogenes, for example tyrosine kinase inhibitors, and immunotherapies like immune checkpoint inhibitors, chemotherapy continues to be the primary choice of treatment for various types of cancer [3]. Lung cancer has been consistently recognized as the most prevalent form of cancer worldwide for several decades [4]. Considerable advancements have been made in comprehending biochemical mechanisms and formulating therapeutic drugs through extensive investigations into the reactivity and interactions between transition metal complexes and biomolecules like DNA and proteins [5,6]. Cisplatin, a platinum-based complex, has been widely used in cancer treatment since its approval for clinical use. It is notable that carboplatin and oxaliplatin are also extensively employed in anticancer therapy [7]. Despite the current achievements of platinum-based medications, they come with a lot of notable constraints. Firstly, their efficacy is confined to a specific spectrum of cancers. Secondly, certain tumors may acquire or possess inherent resistance toward these medications. Lastly, they frequently trigger severe adverse effects including

* Corresponding authors.
E-mail addresses: yany@gd2h.org.cn (Y. Yang), lyjche@gdpu.edu.cn (Y. Liu).
[1] These authors contribute equally.

https://doi.org/10.1016/j.jinorgbio.2024.112652
Received 14 April 2024; Received in revised form 29 May 2024; Accepted 25 June 2024
Available online 26 June 2024

queasiness, suppression of bone marrow function, and toxicity in the kidneys. In recent times, the demand for metal-based compounds in cancer treatment has been on the rise. Photodynamic therapy (PDT) is a minimally invasive procedure that has gained clinical approval and demonstrates selective cytotoxic activity against malignant cells. This technique involves using a photosensitizer followed by exposure to light at a wavelength corresponding to the sensitizer's absorbance band. In the existence of oxygen, this gives rise to a sequence of occurrences that lead to prompt demise of tumor cells, impairment to the microvascular system, and stimulation of localized inflammatory reactions [8]. With the advent of recent technological progressions, photodynamic therapy (PDT) exhibits immense promise in becoming widely adopted for cancer treatment.

Iridium(III) polypyridine complexes have been utilized in cancer therapy due to their exceptional anti-tumor activity and precise organelle targeting [9–11]. Recently, iridium(III) metal complexes have surfaced as promising contenders for innovative metallodrugs with potential anticancer properties due to their capacity to exhibit exceptional anticancer efficacy through various mechanisms, such as hindering protein activity related to biological processes [12,13], catalyzing redox reactions within cells [14,15], and interacting with DNA [16].

In our prior research, we discovered that a lot of iridium(III) complexes exhibit distinctive mechanism against cancer, including disruption of mitochondrial function, interaction with DNA, enhancement of reactive oxygen species (ROS), evoking immunogenic cell death, triggering endoplasmic reticulum stress, and discharge of cytochrome *c* [17–21]. More notably, we have discovered the iridium(III) complex, which functions as a photosensitizer in photodynamic therapy (PDT), $^3O_2$ (trilinear state) can be transferred into $^1O_2$ (singlet oxygen), thereby inducing cancer cell apoptosis [22,23].

In this study, we designed three ligands and their iridium(III) metal complexes $[Ir(ppy)_2(BDIP)](PF_6)$ (BDIP = 2-(6-bromobenzo[d][1,3]dioxol-5-yl)-1H-imidazo[4,5-f][1,10]phenanthroline, ppy = deprotonated 2-phenylpyridine) (3a), $[Ir(ppy)_2(MDIP)](PF_6)$ (MDIP = 2-(7-methoxybenzo[d][1,3]dioxol-5-yl)-1H-imidazo[4,5-f][1,10]phenanthroline) (3b) and $[Ir(ppy)_2(NDIP)](PF_6)$ (NDIP = 2-(6-nitrobenzo[d][1,3]dioxol-5-yl)-1H-imidazo[4,5-f][1,10]phenanthroline (3c). These complexes were characterized through HRMS and NMR spectra. The anticancer effectiveness of the complexes against BEL-7402, HepG2, HeLa, A549, Huh 7 and non-cancer NIH3T3 cells was investigated in detail.

2. Experimental

2.1. Materials and methods

$IrCl_3{\cdot}3H_2O$ was procured from Kunming Boren Precious Metals Co., LTD, 2-phenylpyridine, 6-bromobenzo[d][1,3]dioxole-5-carbaldehyde, 5-methoxybenzo[d][1,3]dioxole-5-carbaldehyde and 6-nitrobenzo[d][1,3]dioxole-5-carbaldehyde were sourced from HERK Chemical Co., LTD (Beijing). Additionally, Guangzhou Chemical Reagent Factory provided the 1,10-phenanthroline. The Fetal Bovine Serum (FBS) and Dulbecco's Modified Eagle Medium (DMEM) were procured from Gibco. BEL-7402 (human hepatocellular), HepG2 (human hepatocellular), HeLa (human cervical), A549 (human lung cancer), Huh7 (human liver cancer) and NIH3T3 (mouse embryonic fibroblasts) cells were obtained from the Cell Center of Sun Yat-Sen University (Guangzhou, China).

The HRMS analysis was performed on Xevo G2-XS QT mass analyzer (Waters, USA) by directly injecting the sample. The NMR spectra were obtained on a Varian-500 spectrometer (500 MHz), DMSO-d_6 and tetramethylsilane (TMS) were used as solvent and internal standard. UV-2700 ultraviolet spectrophotometer (Shimadzu, Japan) and F-2500 fluorescence spectrophotometer (Hitachi, Japan) were utilized to determine the UV–Vis and fluorescence spectra.

2.2. Synthesis of ligands and complexes

2.2.1. Preparation of BDIP, MDIP and NDIP

2-(6-nitrobenzo[d][1,3]dioxol-5-yl)-1H-imidazo[4,5-f][1,10]phenanthroline (NDIP) was synthesized according to the literatures [24]. 2-(6-bromobenzo[d][1,3]dioxol-5-yl)-1H-imidazo[4,5-f][1,10]phenanthroline (BDIP) and 2-(7-methoxybenzo[d][1,3]dioxol-5-yl)-1H-imidazo[4,5-f][1,10]phenanthroline (MDIP) were prepared as following: 1,10-phenanthroline-5,6-dione (0.42 g, 2.0 mmol), 6-bromobenzo[d][1,3]dioxole-5-carbaldehyde or 5-methoxybenzo[d][1,3]dioxole-5-carbaldehyde (2.0 mmol, 0.36 g), and NH_4Ac (40.0 mmol, 3.08 g) and glacial CH_3COOH were refluxed at 130 °C for 2 h, thereafter, the solution was neutralized with concentrated $NH_3{\cdot}H_2O$ and a yellow precipitate washed with ice water was gained.

BDIP: Yield: 75%. Analytical calcd for $C_{20}H_{11}N_4BrO_2$: C, 57.30; H, 2.64; N, 13.36%. Found: C, 57.08; H, 2.89%; N, 13.55%. HRMS (CH_3CN): m/z = 419.0133. ^{1}HNMR (DMSO-d_6, 500 MHz): δ 9.05 (dd, J = 1.5, J = 4.0 Hz, 2H), 8.86 (dd, J = 2.0, J = 8.5 Hz), 7.84–7.81 (m, 2H), 7.48 (s, 1H), 7.41 (s, 1H), 6.22 (s, 2H).

MDIP: Yield: 79%. Analytical calcd for $C_{21}H_{14}N_4O_3$: C, 68.10; H, 3.81; N, 15.13%. Found: C, 68.35; H, 3.66%; N, 15.25%. HRMS (CH_3CN): m/z = 386.0879. ^{1}HNMR (CD_3OD, 500 MHz): 8.85–8.83 (m, 2H), 8.55 (s, 2H), 7.57–7.55 (m, 2H), 7.19 (s, 1H), 7.02 (s, 1H), 5.96 (s, 2H), 3.91 (s, 3H).

2.2.2. $[Ir(ppy)_2(BDIP)](PF_6)$ (3a)

The precursor cis-$[Ir(ppy)_2Cl]_2$ [25] was synthesized using $IrCl_3{\cdot}3H_2O$ and 2-phenylpyridine as starting materials. Cis-$[Ir(ppy)_2Cl]_2$ (0.5 mmol, 0.536 g) and BDIP (1.0 mmol, 0.419 g) were dissolved in 60 mL of dichloromethane and methanol (*v*/v, 2:1) and refluxed for 6 h, then about 1.5 g NH_4PF_6 powder was added to the above solution and stirred continuously for 1 h. The filtrate was extracted, the solvent was removed, the yellow powder was gained. The crude product underwent purification via alumina column chromatography, and dichloromethane and methanol were used as eluents, and the orange yellow strip was collected, the yellow powder was obtained. Yield: 80%. HRMS (CH_3CN, **Fig. S1**, SI): $C_{42}H_{27}BrN_6O_2PF_6Ir$: m/z = 919.0811 [$(M\text{-}PF_6)^+$]. ^{1}H NMR (500 MHz, DMSO-d_6, **Fig. S2**, SI): δ 9.00 (dd, J = 1.5, J = 8.0 Hz, 2H), 8.26 (d, J = 8.5 Hz, 2H), 7.98–7.95 (m, 4H), 7.90–7.85 (m, 4H), 7.48 (d, J = 7.0 Hz, 2H), 7.41 (s, 1H), 7.33 (s, 1H), 7.05 (t, J = 7.5 Hz, 2H), 7.00 (t, J = 7.5 Hz, 2H), 6.95 (t, J = 7.5 Hz, 2H), 6.32 (d, J = 8.5 Hz, 2H), 6.14 (s, 2H).·^{13}C NMR (125 MHz, DMSO-d_6, **Fig. S3**, SI): δ 172.67, 167.49, 151.83, 149.30, 148.17, 147.26, 146.24, 144.55, 143.16, 138.94, 131.97, 131.77, 130.63, 126.76, 126.72, 125.45, 124.24, 122.59, 120.36, 113.43, 112.87, 111.85, 102.53.

2.2.3. $[Ir(ppy)_2(MDIP)](PF_6)$ (3b)

This complex was synthesized using the same procedure as 3a, with MDIP instead of BDIP. Yield: 85%. HRMS (CH_3CN, **Fig. S4**, SI): $C_{43}H_{30}N_6O_3PF_6Ir$: m/z = 871.2011 [$(M\text{-}PF_6)^+$]. ^{1}H NMR (500 MHz, DMSO-d_6, **Fig. S5**, SI): δ 9.14 (dd, J = 1.0, J = 8.0 Hz, 2H), 8.28 (d, J = 8.5 Hz, 2H), 8.15 (d, J = 5.5 Hz, 2H), 8.09–8.06 (m, 2H), 7.96 (d, J = 7.5 Hz, 2H), 7.89 (t, J = 7.5 Hz, 2H), 7.64 (d, J = 5.0 Hz, 1H), 7.53–7.51 (m, 3H), 7.07 (t, J = 7.5 Hz, 2H), 7.02–6.95 (m, 4H), 6.31 (d, J = 7.5 Hz, 2H), 6.16 (s, 2H), 4.00 (s, 3H). ^{13}C NMR (125 MHz, DMSO-d_6, **Fig. S6**, SI): δ 168.83, 152.55, 150.95, 150.79, 149.44, 145.93, 145.50, 145.43, 140.52, 138.14, 133.98, 133.11, 132.12, 128.37, 126.93, 125.69, 124.18, 121.86, 108.67, 103.71, 102.44, 58.48.

2.2.4. $[Ir(ppy)_2(NDIP)]PF_6$ (3c)

$[Ir(ppy)_2(NDIP)](PF_6)$ (3c) was prepared using the same procedure as 3a, with NDIP instead of ligand BDIP. Yield: 84%. HRMS (CH_3CN, **Fig. S7**, SI): $C_{42}H_{27}IrN_7O_4$: m/z = 886.2736 [$(M\text{-}PF_6)^+$]. ^{1}H NMR (500 MHz, DMSO-d_6, **Fig. S8**, SI): δ 8.95 (d, J = 8.0 Hz, 2H), 8.26 (dd, J = 1.5, J = 8.5 Hz, 2H), 8.02 (d, J = 4.0 Hz, 2H), 7.96–7.85 (m, 6H), 7.61 (s, 1H), 7.58 (s, 1H), 7.50 (d, J = 6.0 Hz, 2H), 7.06 (t, J = 6.5 Hz, 2H), 7.00

(t, $J = 6.0$ Hz, 2H), 6.95 (t, $J = 7.0$ Hz, 2H), 6.32–6.29 (m, 4H). ^{13}C NMR (125 MHz, DMSO-d_6, **Fig. S9**, SI): δ 172.51, 167.42, 151.45, 150.54, 149.42, 147.23, 144.52, 143.82, 143.72, 139.01, 132.09, 131.73, 130.66, 126.70, 125.48, 124.27, 122.67, 120.38, 109.99, 105.46, 103.85.

Note: The procedures for pK_a values determination, lipid-water partition coefficient, cell culture, detection of singlet oxygen production, cellular uptake, scratch wound healing and colony-forming assay, mitochondrial and lysosomes localization, mitochondrial permeability transition pore (MPTP), membrane potential determination (MMP), cytochrome C, cell cycle distribution, apoptosis, autophagy, and measurement of CRT, HSP70, HMGB1, ATP (adenosine triphosphate) can be discovered in the supporting materials.

2.3. Cytotoxicity assay in vitro

The complexes were dissolved in DMSO, the final concentrations of DMSO are <0.05%. The cell viability in the presence of 3a, 3b, 3a (light) and 3b (light) was examined by 3-(4,5-dimethylthiazol-2-yl)-2,5-diphenyltetrazolium (MTT) [26], cisplatin was applied as a positive control. The cancer cells were seeded into 96-well microplates and incubated in a 5% CO_2 incubator at 37 °C for 24 h, then different concentrations of complexes (100 → 1.56 μM) were added to the wells for 48 h, while in the light groups, after a 4 h interaction of 3a, 3b and 3c with cancer cells, then irradiated for 30 min and continuously cultured for 48 h, MTT dye solution (20 μL, 5 mg/mL) was added to each well. After 4 h, 100 μL dimethylformamide (50%) and 20% sodium dodecyl sulfate (20%) was applied to dissolve MTT formazan product, the optical density was measured at 490 nm. Each experiment was performed in triplicate. The cell viability was gained based on the equation:

$$\text{Cell viability}\% = \left(\left(A_{\text{sample}} - A_{\text{medium control}}\right) / \left(A_{\text{cell control}} - A_{\text{medium control}}\right)\right) \times 100$$

Whereas A_{sample}, A_{medium} and A_{blank} are the absorbance values of sample, medium and control.

2.4. Ferroptosis studies

The glutathione (GSH) and glutathione disulfide (GSSG) Assay Kit was applied to determine the amount of reduced GSH. Seeded in a 6-well plate and cultured for 24 h, A549 cells were dealt with IC_{50} concentrations of 3a and 3b for 26 h, while in the light-treated groups, A549 cells were incubated with IC_{50} concentrations of 3a and 3b for 4 h, then irradiation for 30 min and continuously incubated for 26 h. Thereafter, A549 cells were trypsinized, washed three times with PBS (phosphate buffer saline). Glutathione content was determined via measuring absorbance at 412 nm.

In the assay of malondialdehyde (MDA) content, A549 cells, treated with IC_{50} concentrations of 3a and 3b for 26 h upon irradiation or not, were washed three times with PBS and then lysed using a mixture of RIPA (50 mM Tris, pH = 7.4, 150 mM sodium chloride, 1% NP-40, and 0.5% sodium deoxycholate) and PMSF (phenylmethanesulfonyl fluoride). Insoluble cell debris was removed by centrifuging at 15,000*g* at 4 °C for 10 min. Total protein was determined using pierce bicinchoninic acid (BCA) protein assay kit. The lysates obtained were detected with the MDA assay kit. The content of MDA can be obtained by calculating the content of protein and MDA in the solution.

Lipid peroxidation was detected by 4,4-difluoro-5-(4-phenyl-1,3-butadienyl)-4-bora-3a,4a-diaza-s-indacene-3-undecanoic acid (C11-BODIPY) fluorescent probe. A549 cells, treated with IC_{50} concentrations of 3a or 3b for 6 h upon light or without light, were then washed three times and stained with a C11-BODIPY fluorescent probe for 30 min and photographed. Treatment of A549 cells with IC_{50} concentrations of 3a or 3b upon irradiation or not for 26 h, flow cytometry was applied to determine the red and green fluorescence intensity.

2.5. Western blotting assay

Treatment of A549 cells with 3a, 3b upon irradiation or not for 26 h, the concentration of protein in the supernatant was obtained according to BCA (bicinchoninic acid) assay. Amount of the proteins in the per lane is equal in the sodium dodecyl sulfate-polyacrylamide gel electrophoresis. After gel electrophoresis, the gels were transferred to polyvinylidene difluoride membranes (Millipore) and blocked with 5% non-fat milk in TBST (20 mM Tris-HCl, 150 mM NaCl, 0.05% Tween 20, pH 8.0) buffer for 3 h. After washing four times with TBST buffer, the membranes were incubated with primary antibody solution at 4 °C overnight, washing three times again, the secondary antibodies were then conjugated with horseradish peroxidase (1:5000 dilution) for 70 min at room temperature. Finally, the blots were treated with the Amersham ECL Plus western blotting detection reagents.

2.6. Data analysis

The mean ± SD was used to express all data, and *t*-tests were employed to evaluate statistical significance. Significance was determined at a level of $^*P < 0.05$, $^{**}P < 0.01$, $^{***}P < 0.001$.

3. Results and discussion

3.1. Syntheses and characterization

The general procedure for 3a, 3b, 3c is illustrated in Scheme 1, ligands BDIP, MDIP and NDIP were synthesized through condensation of 1,10-phenanthroline-5,6-dione with 6-bromobenzo[d][1,3]dioxole-5-carbaldehyde, 5-methoxybenzo[d][1,3]dioxole-5-carbaldehyde and 6-nitrobenzo[d][1,3]dioxole-5-carbaldehyde. Subsequently, the synthesis of 3a, 3b and 3c was performed via the reaction with $[Ir(ppy)_2Cl]_2$ and BDIP, MDIP, NDIP in a dichloromethane-methanol under argon. With dichloromethane-methanol as eluent, neutral alumina column chromatography was applied to purify 3a-3c. In the HRMS spectra, $[M\text{-}PF_6]^+$ signal was observed which corresponded to the expected molecular weight. Additionally, in the ^{1}HNMR spectra, the signals for the protons in the imidazole ring were not found, the signals at 6.14, 6.16 ppm are assigned to the protons (-CH_2) in the dioxolane of 3a, 3b, whereas the peak of 4.00 ppm for 3b is attributed to the protons (-OCH_3). In the ^{13}CNMR spectra, the signals at 102.53, 102.44 and 103.85 ppm are assigned to the carbon atoms in the dioxolane ring of 3a, 3b, 3c, the peak at 58.48 ppm is attributed to the carbon at -OCH_3. The purity of 3a, 3b and 3c was detected by high performance liquid chromatography (HPLC), methanol was used as mobile phase. As observed from **Fig. S10** (SI), what a main peak was uncovered revealed that pure compounds were gained with a purity value of 96.23, 98.86 and 97.47% for 3a, 3b and 3c.

The UV–Vis spectra of complexes 3a-3c (10.0 μM) in PBS were determined (**Fig. S11a**, SI). The maximum absorbance wavelengths appear at 273 nm (ε = 62,150), 258 nm (ε = 41,100) and 270 nm (ε = 77,290) for 3a, 3b and 3c, respectively. The complexes emit weak green fluorescence (**Fig. S11b**, SI), appearing at 628 nm (λ_{ex} = 273 nm), 627 nm (λ_{ex} = 258 nm), 628 nm (λ_{ex} = 270 nm).

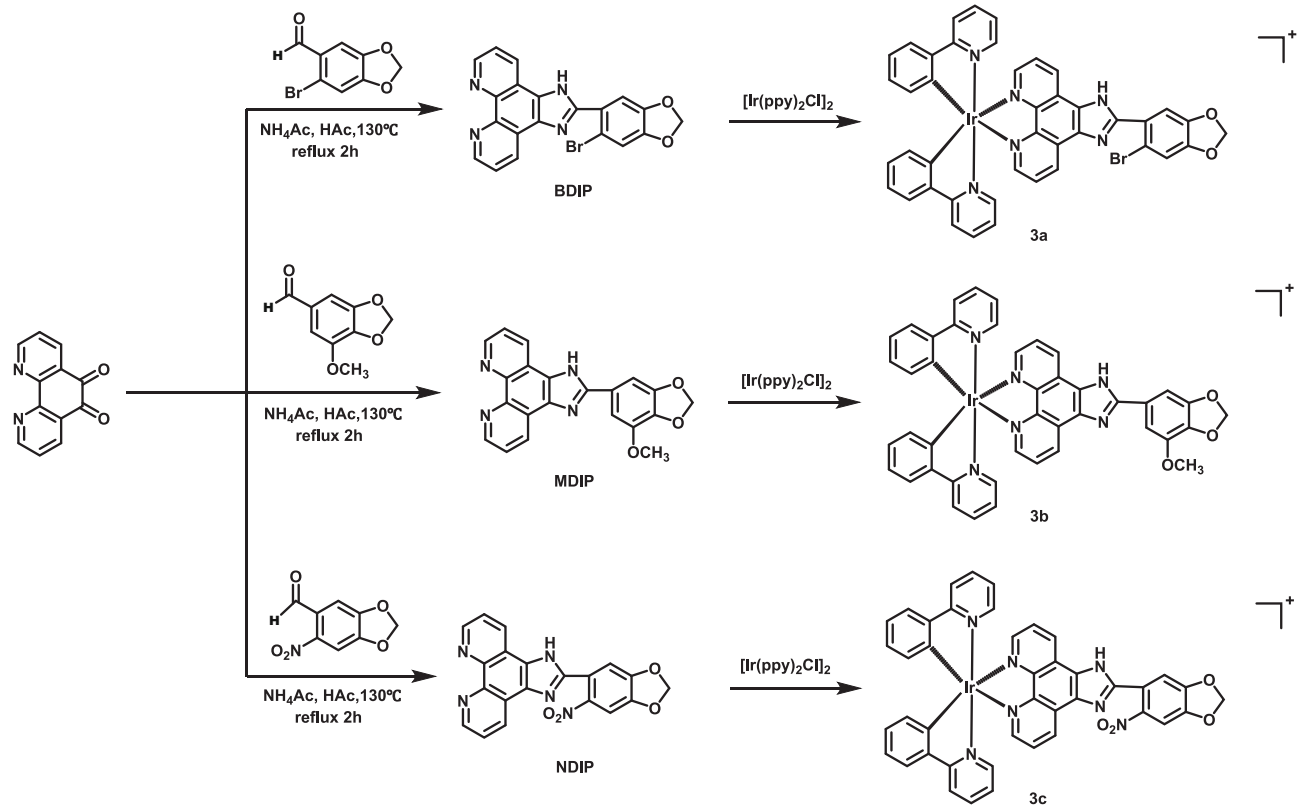

Scheme 1. Synthetic route of BDIP, MDIP, NDIP, 3a, 3b and 3c.

The stability of 3a, 3b and 3c in PBS solution was determined by using UV–Vis spectra. As depicted in **Fig. S12** (SI), at 0 and 24 h, the peak shape has no change, indicating that the complexes are stable.

3.2. *pKa values determination*

Substances that have pK_a values higher than 4 for acids and lower than 10 for bases predominantly charged at physiological pH can cross the blood-brain barrier. The pK_a value of a drug directly affects its lipophilicity, solubility, protein binding, and permeability. Consequently, it has a significant influence on crucial pharmacokinetic characteristics such as absorption, distribution, metabolism, and excretion [27]. The titration curve of 3a-3c is depicted in **Fig. S13** (SI), the pH values of 3a-3c were measured as 6.59, 6.77, and 6.40, respectively, while the pK_a values were determined to be 6.43, 6.85, and 6.05 for 3a, 3b and 3c. Notably, all pK_a values for 3a-3c exceed 4, indicating its potential ability to traverse cell membranes and serve as a potent drug candidate.

Additionally, we determined the lipid-water partition coefficient (logP) using shake flash method [28]. The logP values for 3a, 3b and 3c were measured to be 0.4987, 0.1956 and 0.7833, respectively, indicating that the complexes can enter the cancer cells.

Table 1
IC_{50} values (μM) of 3a, 3b and 3c treating cancer cells for 48 h.

Complex	BEL-7402	HepG2	HeLa	A549	Huh7	NIH3T3
3a	17.1 ± 0.4	9.3 ± 1.7	19.1 ± 1.3	4.0 ± 0.6***	16.6 ± 1.6	16.3 ± 1.7
3a (light)	6.4 ± 0.4	2.8 ± 0.06	19.7 ± 0.8	0.7 ± 0.3**	8.8 ± 1.3	7.3 ± 0.4
3b	> 100	> 200	> 100	26.8 ± 5.7**	> 200	26.8 ± 2.1
3b (light)	43.2 ± 5.7	> 100	> 100	1.8 ± 0.1**	30.0 ± 1.6	11.9 ± 1.0
3c	> 200	> 200	> 200	> 100	34.3 ± 3.4	17.5 ± 0.7
3c (light)	7.3 ± 0.9	> 100	> 200	34.3 ± 1.8*	29.2 ± 3.9	13.9 ± 0.6
Cisplatin	14.8 ± 3.4	9.4 ± 1.5	5.7 ± 1.1	6.6 ± 0.7	nd	nd

Data for cisplatin from Ref [20, 21], *$p < 0.05$, **$p < 0.01$, ***$p < 0.001$.

3.3. *Irradiation increases the cytotoxicity*

In a cytotoxicity study, the average IC_{50} concentrations values of 3a, 3b and 3c against BEL-7402, HepG2, HeLa, A549, Huh7 and non-cancer NIH3T3 cells were determined applying 3-(4,5-dimethylthiazole-2-yl)-2,5-diphenyl tetrazolium bromide (MTT) [26]. The obtained results are presented in Table 1, 3a exhibits moderate anti-tumor activity against BEL-7402, HepG2, HeLa and Huh7 cells. Surprisingly, 3a shows high anticancer efficiency toward A549 cells with a low IC_{50} value of 4.0 ± 0.6 μM, while 3b and 3c display no or low cytotoxic activity on the above cells. To enhance the anti-tumor activity, after the cells were incubated with 3a, 3b or 3c for 4 h, then the cells was subjected to LED lamp (white light, 65 W, λ = 460 nm, 7.03 J/cm^2) exposure of 30 min, 3a-3c demonstrates significant anti-tumor effects, especially, 3a and 3b possess strong antiproliferative ability to prevent A549 cell proliferation with a low IC_{50} value of 0.7 ± 0.3 and 1.8 ± 0.1 μM. Their anticancer activity on A549 cells is higher than that of cisplatin. The complexes show moderate cytotoxic effect on non-cancer NIH3T3 cells. Among the three complexes, upon irradiation, 3a as Br atom as substitute shows the highest cytotoxic effect on all the selected cancer cells, this may be caused by the strongest ability to produce ROS.

To investigate the reason for different cytotoxicity of 3a, 3b and 3c toward cancer cells under white light, we determined the singlet oxygen ($^1O_2$) and quantum yield Φ.

When combined with $^1O_2$, 1,3-diphenylisobenzofuran (DPBF) is irreversibly oxidated to form 1,2-dibenzoylbenzene, the absorbance deceases. As shown in **Fig. S14** (SI), the absorbance of DPBF at 411 nm

reduced by 76.0% for 3a, 66.3% for 3b and 48.6% for 3c, respectively, hence, 3a as Br atom as substitute exhibits the strongest ability to produce singlet oxygen among these complexes. These results indicating that the complexes can produce singlet oxygen which further leads to cancer cell death.

In addition, the quantum yield Φ were calculated from the following Eq. [29]:

$$\Phi_{sample} = \Phi_{Ref} \times \left(K_{sample}/K_{Ref}\right) \times \left(F_{Ref}/F_{sample}\right)$$

K is the slope, F is calibration factor of the absorbance, $F = 1–10^{-OD}$ (OD is the absorbance of the photosensitizer at the light source wavelength). $[Ru(bpy)_3]^{2+}$ was used as a reference ($\Phi = 0.81$, methanol) [30]. The quantum yields Φ for 3a, 3b and 3c were determined to be 0.814, 0.679 and 0.382, respectively. The quantum yield of 3a is the largest among the three complexes, hence, 3a exhibits higher anticancer activity than 3b and 3c.

We also applied Gaussian 09 package [31] at the level of B3LYP density functional in conjunction with the 6-31G(d) basis sets for C, H, N, O, Br, atoms, LanL2DZ for Ir atom to calculate the energy of the lowest unoccupied orbital (LUMO) and the highest occupied orbital (HOMO) to verify the cytotoxic order of 3a > 3b. In general, small ΔE value between LUMO and HOMO will result in easy deformation of the electron cloud corresponding to high anticancer activity. As depicted in Fig. 1, the ΔE values are 2.6207 eV for 3a, 2.7712 eV for 3b, respectively. The ΔE value of 3a is smaller than that of 3b, indicating that the cytotoxic activity of 3a is higher than those of 3b, which is consistent with the cytotoxic activity of these complexes. Similar results were found in the other iridium(III) complexes [32,33].

Owing to 3c exhibiting low cytotoxicity on A549 cells, in the following cell experiments, 3a and 3b were used to explore the anticancer efficiency on A549 cells.

3.4. Cellular uptake, cell colonies and wound healing studies

Understanding the mechanisms underlying the interaction between complexes and cells, as well as their impact on cellular uptake, is crucial for exploring the biomedical applications of complexes, particularly in drug delivery. Various factors, such as disparities in complex physical properties or alterations in cell membrane characteristics, can influence the process of interaction and uptake by cells [34]. Treatment of A549 cells with 3a and 3b (IC_{50} concentrations) for 6 h, we employed image Xpress Micro XLS to investigate cell uptake and determine whether the complexes could penetrate in the cells. Due to inherent properties of the complex itself, both 3a and 3b were able to emit green fluorescence while 4′,6-diamidino-2-phenylindole (DAPI) staining rendered nuclei blue. The overlapping signals from green and blue fluorescence indicate that both 3a and 3b possess a strong capability to efficiently enter cells and mainly distribute within their cytoplasm (Fig. 2a).

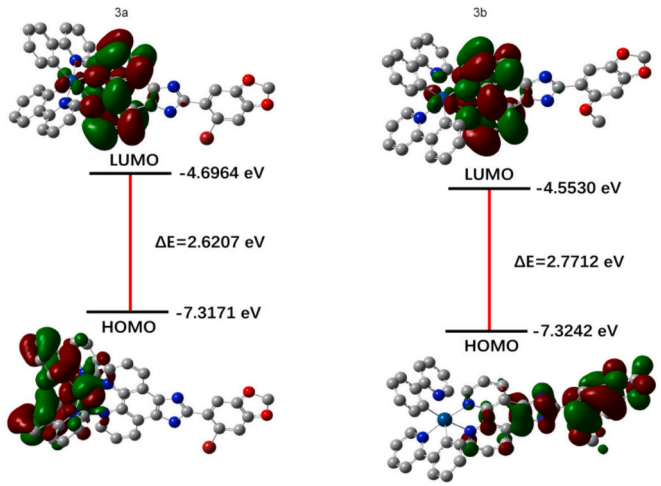

Fig. 1. The energy of LUMO and HOMO of 3a and 3b.

To quantify the cellular uptake, cancer A549 cells were cultured with 3a or 3b (IC_{50} concentration) for 26 h, the results obtained are presented in Fig. 2b. Compared to that in the control group, the treated groups exposed to 3a, 3b, 3a (light) and 3b (light) exhibited a different degree increase in green fluorescence intensity, further indicating their excellent ability to penetrate cells. These findings suggest that both 3a and 3b possess remarkable cell penetration capabilities as well as cytoplasmic distribution.

Colony formation is an effective method for assessing the complexes to prevent the cell proliferative capacity, and this can be quantified by calculating the colony formation rate. Following exposure to IC_{50} concentrations of 3a and 3b for 7 days (Fig. 2c), the number of A549 cells decreased by 33.3% and 36.3% compared to that in the control. However, under irradiation, there was a significant reduction in cell numbers by 81.5% for 3a and 80.9% for 3b, respectively (**Fig. S15a**, SI). These results affirm that both 3a and 3b effectively suppress A549 cell proliferation.

Tumor metastasis is a complex process involving a series of changes, including cell migration, invasion, tumor growth, and angiogenesis. Observing from Fig. 2d, after exposure of A549 cells to 3a or 3b for 26 h, the number of cells decreased by 10.8% and 23.4%. On the other hand, upon irradiation, the number of cells decreased by 28.5% for 3a and 35.1% for 3b (**Fig. S15b**, SI). The findings hint that 3a and 3b effectively inhibit A549 cell migration.

The focal adhesion kinase (FAK) is a highly phosphorylated kinase during cell adhesion, playing a pivotal role in tumor invasion and metastasis [35,36]. In patients, elevated FAK expression is associated with poor prognosis and resistance to certain major treatments [37]. As depicted in Fig. 2e, both 3a and 3b downregulated the expression of FAK protein. These findings once again substantiate that both 3a and 3b possess significant capability to inhibit A549 cell migration.

3.5. Cell cycle arrest analysis

If there is DNA damage, the cell cycle will stop at appropriate checkpoint, and cell cycle arrest gives cell additional time to repair the damage, thus reducing the mutations and preventing the development of tumors [38]. To explore the complexes to block the cell growth at G0/G1, S or G2/M phase, the cell cycle distribution was studied. See from Fig. 3a, the percentage of cells in the control was 67.58% in the G0/G1 stage, 28.51% in the S stage, and 5.90% in the G2/M stage. In the 3a, 3b, 3a (light), 3b (light) treatment groups, an increase in the cell at the S phase of 12.86% for 3a, 14.47% for 3b, 18.29% for 3a (light) and 23.57% for 3b (light) was found, which suggests that 3a and 3b block the cell growth at S phase. Upon irradiation, 3a (light) and 3b (light) show higher efficiency than 3a and 3b without light.

The regulation of the cell cycle involves cyclins, serine or threonine cyclin-dependent kinases (CDKs) [39]. Cyclin B1 and cyclin A2 predominantly expressed in the S and G2/M phases. Since the formation of a complex between cyclin proteins and CDK proteins is necessary for regulating the cell cycle, we also analyzed CDK2 and CDK4 proteins. As depicted in Fig. 3b, the expression of cyclin B1, cyclin A2, CDK2, and CDK4 proteins were validly inhibited. These findings suggest that 3a and 3b primarily induce cell stasis in the S phase through reduced expression of cyclin B1, cyclin A2, CDK2, and CDK4. Taken together, these results unveil that 3a and 3b block proliferation in A549 at the S phase.

3.6. Localization, mitochondrial permeability transition pore and membrane potential determination

In addition to biological energy functions, mitochondria play a crucial role in regulating cell death, maintaining ion homeostasis, oxidizing carbohydrates and fatty acids, as well as participating in

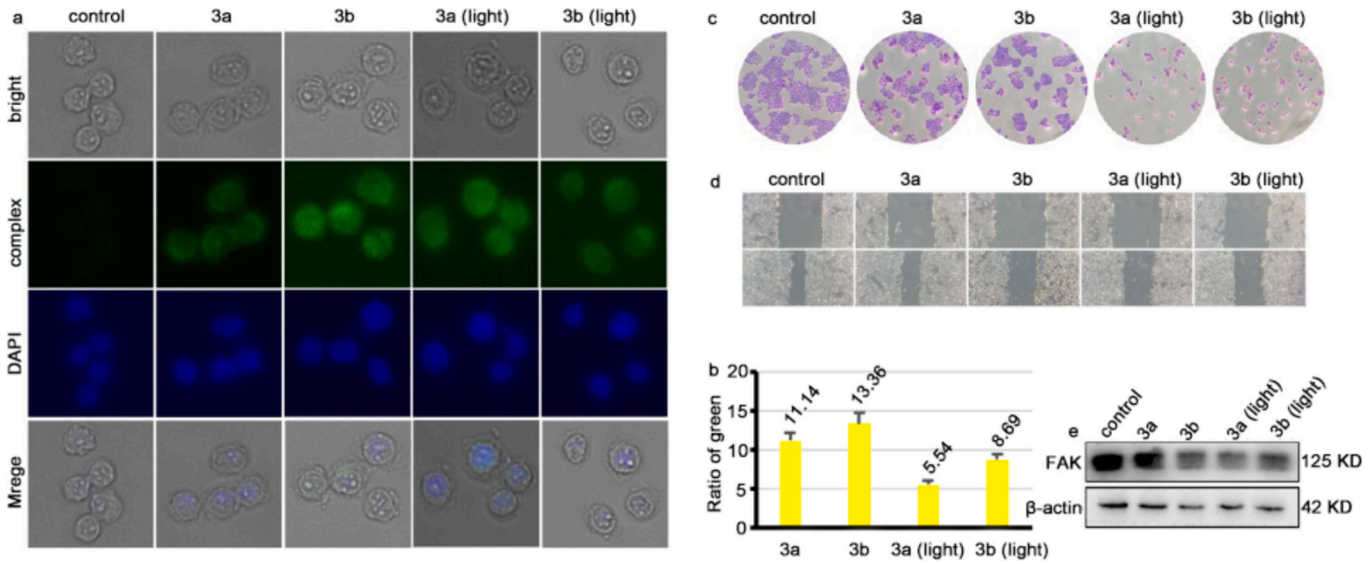

Fig. 2. (a) Cellular uptake of a 6 h exposure of A549 cells to IC_{50} concentrations of 3a, 3b, 3a (light) and 3b (light). (b) Ratio of green fluorescence, (c) colony formation, (d) wound healing assay, (e) expression of FAK protein while A549 cells were exposed to IC_{50} concentrations of 3a, 3b, 3a (light) and 3b (light) for 26 h.

various catabolic and anabolic pathways [40]. Studies have demonstrated that organometallic complexes possess the ability to specifically target organelles such as mitochondria and lysosomes, leading to cellular dysfunction and subsequent organelle damage [41]. The localization of these complexes at the mitochondria and lysosomes was determined using Mito Tracker Deep Red and Lyso-Tracker Red probes. Observe from Fig. 4a and b, 3a and b emitted green fluorescence, lysosomes and mitochondria were dyed red, merge of red and green indicated that 3a, 3b successfully entered A549 cells and acted on the mitochondria and lysosomes. Pearson's colocalization coefficients (PCC) were calculated based on the red and green fluorescence in 50 cells by Image pro plus 6.0 software according to literature [42]. For lysosomes, the PCC values are 0.9882 for 3a, 0.9880 for 3b, 0.9976 for 3a (light), and 0.9989 for 3b (light). For mitochondria, the PCC values are 0.9808 for 3a, 0.9951 for 3b, 0.9934 for 3a (light), and 0.9976 for 3b (light), these results demonstrate that the positive correlations exist.

Interaction of mitochondria will lead to an open of mitochondrial permeability transition pore (MPTP), the MPTP opening has been linked to a lot of types of neuronal demise, apoptosis, ischemia-induced cell death, excitotoxicity-related damage, and neurotoxicity [43]. Normally, MPTP is turned off and $CoCl_2$ cannot enter mitochondria. On the contrary, after the complexes act on the mitochondria, which induces a large amount of extracellular Ca^{2+} to enter cells, resulting in mitochondrial calcium overload and passive MPTP opening. Observe from Fig. 4c and d, a bright green fluorescence was uncovered (control). However, the green fluorescence reduced (lonomycin, positive control; 3a, 3b, 3a (light) and 3b (light)-treated groups). This is because $CoCl_2$ can enter the mitochondria to bind calcein AM and further lead to fluorescence quenching after an open of mitochondrial permeability transition pore. Hence, a decrease in the green fluorescence indicated that 3a and 3b may lead to an open of mitochondrial permeability transition pore.

Mitochondrial membrane potential serves as a sensitive indicator of mitochondrial damage, primarily occurring as an early event in the intrinsic pathway of mitochondrial cell death. It plays a crucial role in maintaining physiological ATP production through the electron transport chain, while significant loss of mitochondrial membrane potential leads to energy depletion and subsequent cell demise [44]. To access the impact of 3a and 3b on mitochondrial damage, we employed 5,5′-6,6′-tetrachloro-1,1′-3,3′-tetramethylbenzomethylene carbon cyanide iodide (JC-1) as fluorescent probes to assess alterations in mitochondrial membrane potential using the complexes as references to rule out disruption on the green fluorescence. It is well known that the red fluorescence stands for high mitochondrial membrane potential (MMP), green fluorescence indicates a low MMP. As depicted in Fig. 4e, bright red (monomer) and poor green fluorescence (aggregates) was discovered corresponding to high MMP (control), while in the cisplatin (positive), 3a, 3b, 3a (light) and 3b (light)-treated groups, we uncovered a reduced red and an increasing green fluorescence corresponding to low MMP. The ratio of red/green fluorescence was measured and depicted in Fig. 4f, the results further affirm that 3a and 3b can effectively cause a reduction in MMP. In summary, these findings suggest that 3a and 3b interact on the mitochondria, lead to mitochondrial damage and ultimately cause apoptosis.

3.7. Studies of intracellular cytochrome c level

In addition to its involvement in electron transfer, cytochrome *c* also plays an important role in apoptosis [45] and is essential for caspase-mediated apoptosis [46]. Therefore, it is imperative to detect intracellular cytochrome *c* level. As depicted in **Fig. S16a** (SI), poor green fluorescence was seen in the blank. However, after treatment with 3a, 3b, 3a (light) and 3b (light) (IC_{50} concentration) for 6 h, we observe obvious green fluorescence, which hinted that cytochrome *c* was liberated from the mitochondria. Subsequently, a high-content analysis system was used to quantitatively detect the content of cytochrome *c*, as shown in **Fig. S16b** (SI), green fluorescence enhances compared with that in the control. These findings demonstrated that iridium(III) metal complexes lead to mitochondrial dysfunction, finally prompt the liberation of cytochrome *c* from the mitochondria.

3.8. Apoptosis and apoptotic mechanism studies

Programmed cell death, also known as apoptosis, is a natural process that eliminates senescent cells. Many treatments for cancer activate pathways that induce apoptosis and lead to the elimination of malignant cells. However, when the signals that control apoptosis are disrupted, particularly when the anti-apoptotic system is triggered, it enables cancer cells to evade this natural process of cell death. As a consequence, uncontrolled cell division occurs, leading to tumor survival and resistance to treatment, ultimately resulting in the recurrence of cancer [47]. See from Fig. 5a, the early apoptotic rate was 2.21% (control). After treating A549 cells with IC_{50} concentration of 3a and 3b for 26 h, the early apoptosis rates in the 3a and 3b-treated groups only increased by

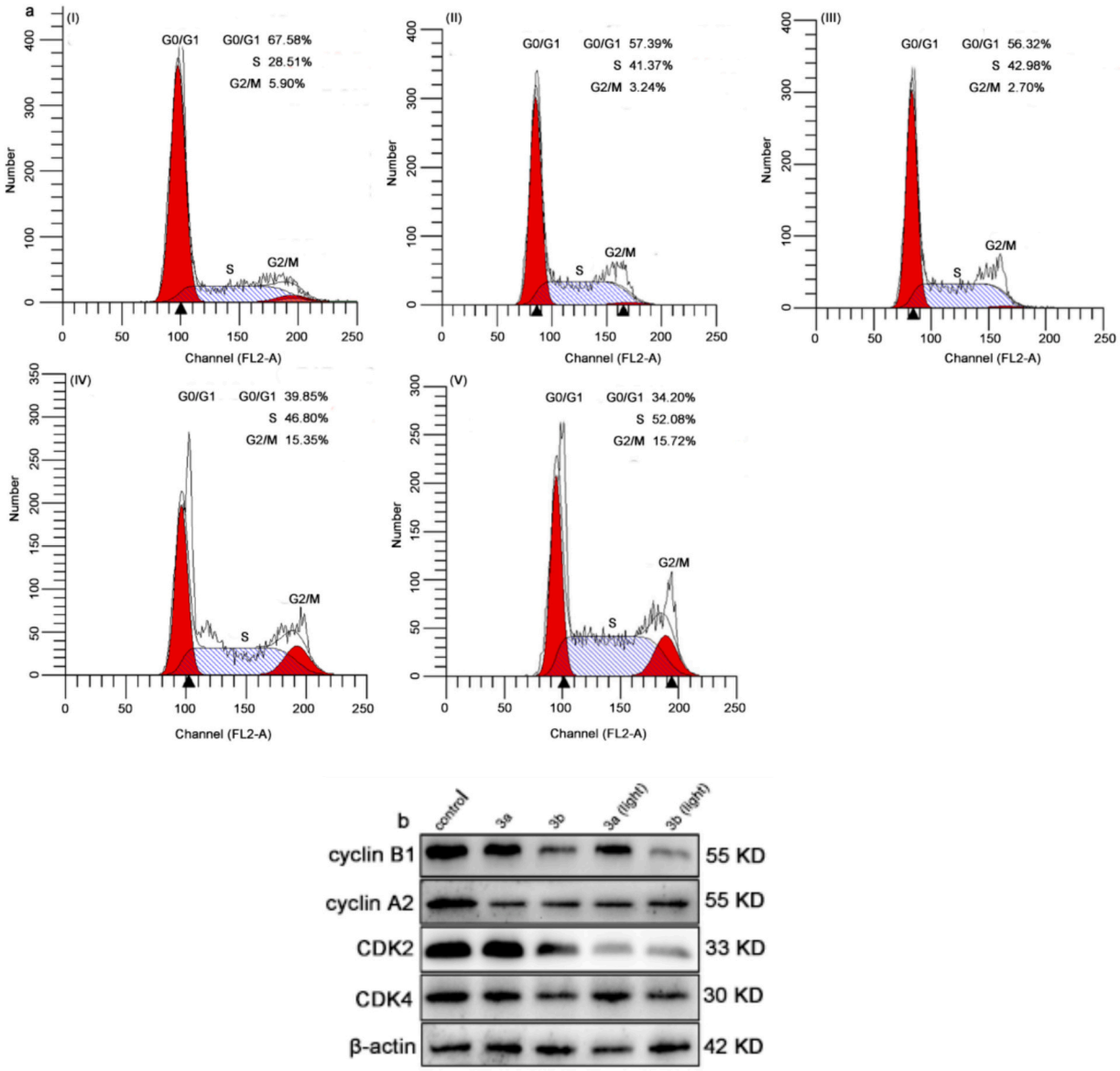

Fig. 3. (a) The distribution of A549 (I) cell cycle and (b) the expression of CDK2, CDK4, cyclin A2, and cyclin B1 after a 26 h of treatment with 3a (4.0 μM, II), 3b (26.8 μM, III), 3a (light) (0.7 μM, IV) and 3b (light) (1.8 μM, V).

4.89% and 3.19%, respectively. However, upon irradiation, the early apoptosis rate caused by 3a (light) and 3b (light) was increased by 14.19% and 7.89%, respectively. The results showed that 3a and 3b could effectively induce the early apoptosis of A549 cells upon irradiation.

Pharmaceuticals or therapeutic approaches that can normalize apoptosis signaling pathways hold the potential to eradicate cancer cells, as they heavily depend on these abnormalities for survival [48]. The PI3K/AKT/mTOR (PI3K: phosphoinositide 3 kinase; AKT: Protein Kinase B; mTOR: mammalian target of rapamycin) signaling pathway plays a crucial role in promoting malignant processes and conferring drug resistance among individuals diagnosed with solid tumors [49]. The growth and progression of colorectal cancer (CRC) are significantly influenced by the PI3K/AKT/mTOR pathway [50]. Poly ADP-ribose polymerase 1 (PARP-1) is an enzyme that binds to DNA and plays a role in DNA damage, programmed cell death, and maintaining genetic integrity [51]. PARP is indispensable in apoptosis [52]. The activation of a cascade of caspase enzymes characterizes the executive stage of apoptosis. Caspase-3 is believed to initiate proteolysis in the process of apoptosis execution, while also serving as a crucial regulator for cellular growth and homeostasis in both normal and malignant tissues within multicellular organisms [53]. The B-cell lymphoma/leukemia-2 (Bcl-2) protein family, consisting of pro-apoptotic and anti-apoptotic proteins, plays an important role in apoptosis regulation, especially through intrinsic pathways, as they are upstream of irreversible cell damage and primarily act on mitochondria, in which Bcl-2-associated X (Bax) also has pro-apoptotic effects [54]. p38 mitogen-activated protein kinase (p38 MAPK) is often activated by a lot of environmental stress stimuli and cytokines that cause inflammation. Excessive inflammation can lead to many diseases, including cancer [55]. Vascular endothelial growth factor (VEGF) is an important regulator of angiogenesis and can be involved in regulating the apoptosis of vascular endothelial cells [56], playing a key role in the malignant behavior of breast cancer cells [57]. Therefore, western blotting was employed to analyze key proteins associated with the intrinsic apoptotic pathway. Observe from Fig. 5b, following a 26 h process with 3a, 3b on irradiation or not, the down-regulation of PARP, caspase 3, and VEGFA were observed. Furthermore, there was a reduction in the expression levels of PI3K, AKT, mTOR, p-mTOR, and Bcl-2, notably more significant reductions were observed in the light-treated group. Additionally, we also found that the

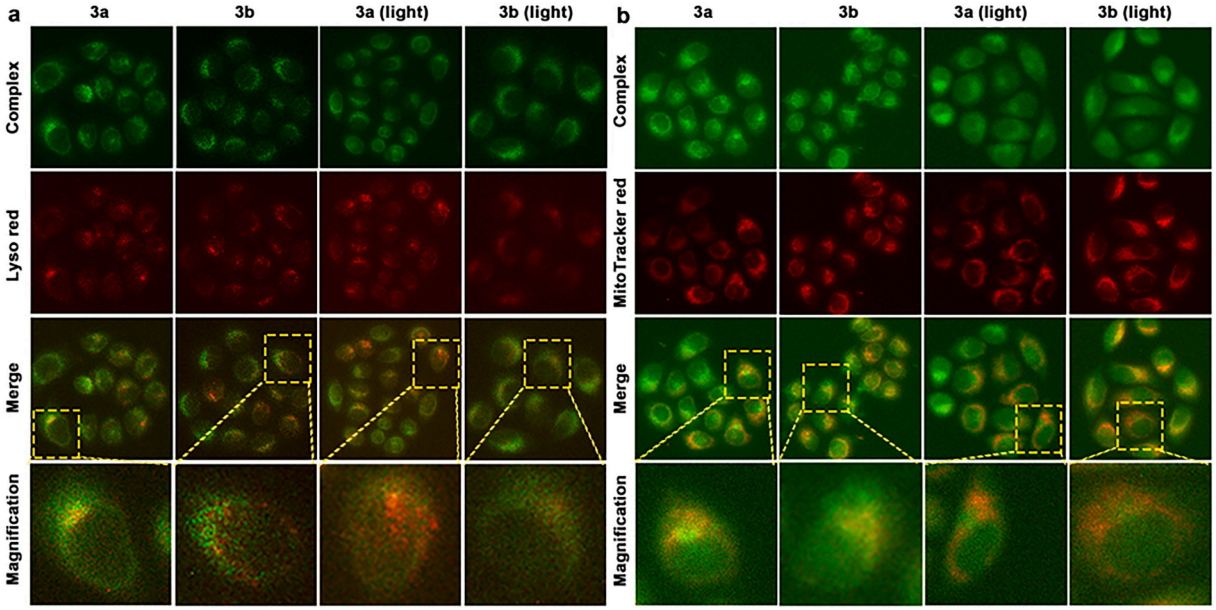

Fig. 4. Co-location of the complexes in the lysosomes (a) and mitochondria (b), (c) mitochondrial permeability transition pore (MPTP) open, (d) green fluorescence intensity, (e) change of mitochondrial membrane potential, (f) the ratio of red/green fluorescence intensity. (For interpretation of the references to colour in this figure legend, the reader is referred to the web version of this article.)

expression levels of p38 MAPK and Bax increased. These findings indicate that 3a and 3b cause apoptosis via hindrance of PI3K/AKT/mTOR and intrinsic apoptotic signaling pathways mediated by mitochondria.

3.9. Detection of ferroptosis

Ferroptosis is an emerging mechanism of cellular demise characterized by lipid peroxidation that is reliant on iron [58,59]. The primary features of Ferroptosis include the elevation in malondialdehyde (MDA) concentration, reactive oxygen species (ROS) level, and Fe^{2+} level, along with a reduction in glutathione (GSH) content [60]. The GSH (reduced glutathione) and MDA levels were assessed using the GSH and GSSG Assay Kit as well as the MDA assay kit (Beyotime Biotechnology, China), respectively. Observe from Fig. 6a and b, we found that the level of GSH reduced, MDA amounts increased after an incubation of A549 cells with 3a, 3b, 3a (light), 3b (light) for 26 h. The results suggest that 3a, 3b can reduce GSH concentration, increase MDA amounts, resulting in a sustained oxidative stress response.

p53 governs the expression of a range of genes responsible for upholding equilibrium within the body, encompassing those implicated in regulating the progression of cell cycles, maintaining redox balance, facilitating DNA replication and mending, orchestrating programmed cell death, and promoting cellular self-degradation [61–63]. Protein immunoblotting was applied to measure p53 expression, and the results were depicted in Fig. 6c, we found that the expression of p53 increased, which further substantiates that 3a, 3b can induce oxidative stress through p53 pathway and eventually lead to apoptosis.

The main cause of lipid peroxidation in ferroptosis is the depletion of glutathione peroxidase 4 (GPX4) levels. GPX4, a selenium-dependent enzyme that relies on glutathione (GSH), plays a crucial role as a phospholipid hydroperoxidase and effectively suppresses the production of lipid ROS [64]. C11-BODIPY dye can transform its fluorescence from red to green after reacting with lipid free radicals produced during lipid peroxidation, which is applied to evaluate the level of lipid peroxidation in the ferroptosis. Observe from Fig. 6d, after A549 cells were dealt with IC_{50} concentration of 3a, 3b, 3a (light), 3b (light), the green fluorescence intensity is enhanced, while the red fluorescence intensity is reduced. The quantitative analysis of red/green ratio showed that the red/green ratio was reduced (Fig. 6e), further hinting that 3a, 3b, 3a (light) and 3b (light) caused a high degree of lipid peroxidation.

Ferrostatin-1 (Fer-1), a well-established ferroptosis inhibitor, has gained significant popularity for its extensive utilization [65,66]. The inhibitory effect of Fer-1 on ferroptosis is mainly dependent on the inhibition of lipid peroxidation [67]. To assess whether increasing lipid peroxidation inducing ferroptosis, we used Fer-1 to evaluate the change in the cell viability. As shown in Fig. 6f, after the cells were pretreated with Fer-1 and 3a, 3b, 3a (light), 3b (light) for 36 h, the cell viability increases compared with those caused by 3a, 3b, 3a (light), 3b (light) alone. These results suggested that the increasing lipid peroxidation may induce ferroptosis.

Iron is an essential element needed by cells and is thought to be a key factor in ferroptosis. Ferritin acts as an essential iron storage protein in cells, forming polymers with crystalline iron nuclei [68]. Ferritin plays an important role in preventing cardiac ferroptosis and subsequent heart failure [69]. As shown in Fig. 6g, compared with that in the control, the expression levels of glutathione peroxidase 4 (GPX4) and Ferritin were downregulated. In summary, reduction of GSH, increase of MDA, decrease in the ratio of red/green dyed by C11-BODIPY, enhancement of cell viability in the presence of Fer-1 and downregulation of Ferritin and GPX4 together affirm that the complexes promote A549 cell death by inducing the ferroptosis pathway.

3.10. Autophagy studies

Not only is there significant crosstalk between autophagy and various cell death modes, but autophagy also modulates mitochondrial recycling, thereby regulating hepatocyte apoptosis through the mitochondrial pathway [70]. Autophagy contributes to the overall degradation of cytoplasm and mitochondria [71,72]. Activation of the autophagy pathway boosts ferroptosis by facilitating ferritin degradation [73]. To investigate whether the complexes can induce autophagy, we employed fluorescent eosinophilic dye monodansylcadaverine (MDC) to detect autophagosome formation. The results are presented in Fig. 7a, green fluorescence was observed in the 3a, 3b, 3a (light), 3b (light)-treated groups, moreover, we observed a lot of autophagic vacuoles, indicating that complexes 3a, 3b, 3a (light), 3b (light) can validly

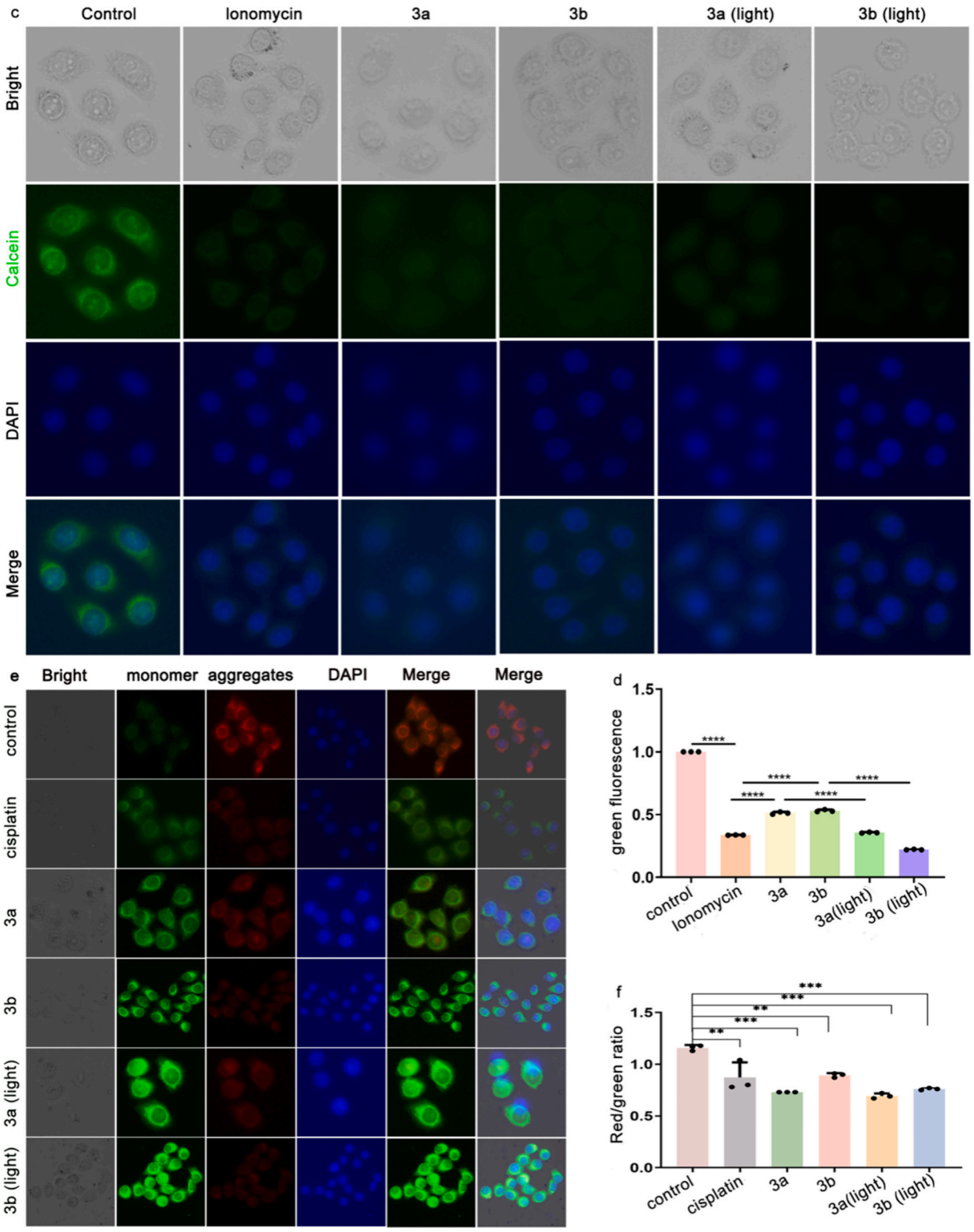

Fig. 4. (*continued*).

induce autophagy. Quantitative analysis of green fluorescence intensity showed a significant increase in the green fluorescence intensity (Fig. 7b).

Beclin-1 is a crucial component in the autophagy pathway, involved in various stages from autophagosome formation to their extension and maturation [74,75]. Beclin-1 plays a central role in regulating autophagy and holds potential as a target for tumor therapy through autophagy modulation [76]. p62 is a multifunctional scaffold protein that participates in the regulation of multiple signaling pathways and autophagy processes. Specifically, p62 acts as an essential adapter responsible for recognizing and delivering specific organelles and protein aggregates to the autophagosome for degradation, known as selective autophagy [77]. To further affirm the occurrence of autophagy, we employed western blot technology to examine the expression of Beclin-1 and p62. Fig. 7c demonstrated an increase and a reduction in the expression of Beclin-1 and p62 proteins, respectively. These findings

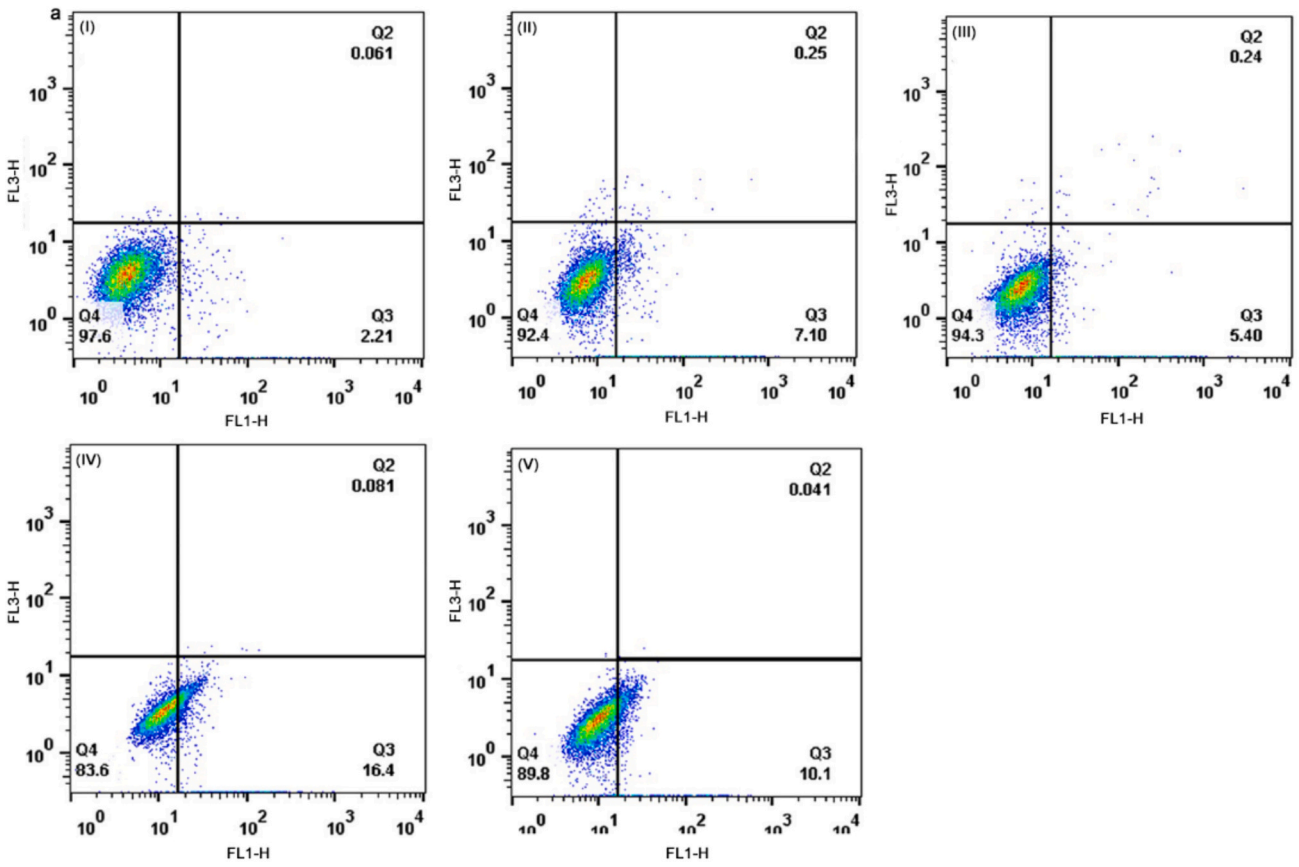

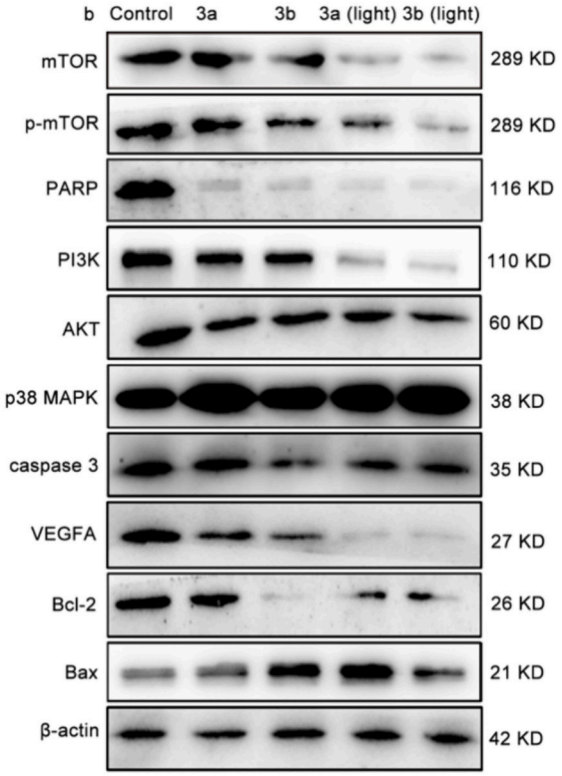

Fig. 5. (a) The apoptosis in A549 cells (I) and (b) expression of PARP, PI3K, AKT, caspase 3, Bcl-2, p38 MAPK, VEGFA, mTOR, p-mTOR, and Bax after exposure to 3a (4.0 μM, II), 3b (26.8 μM, III), 3a (light) (0.7 μM, IV) and 3b (light) (1.8 μM, V) for 26 h.

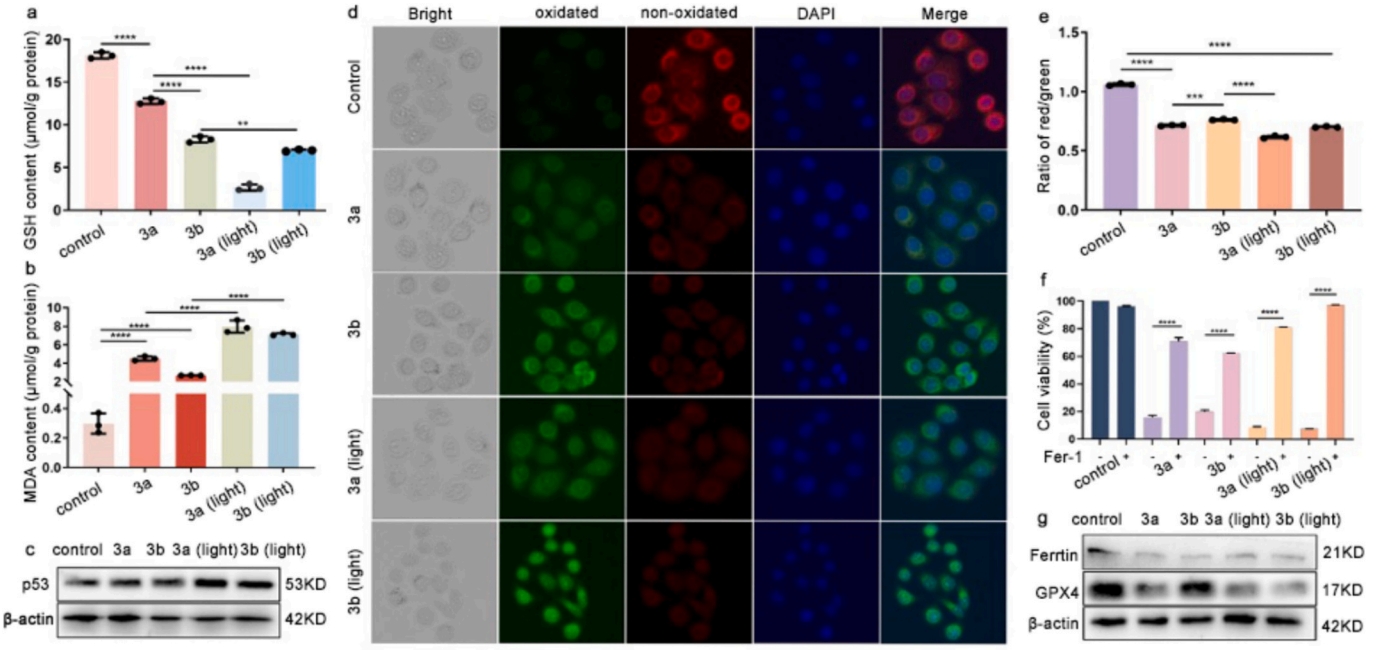

Fig. 6. Measurement of GSH (a), and MDA levels (b), (c) Expression of p53 protein, (d) Detection of lipid-peroxidation using C11-BODIPY as fluorescence probe, (e) Ratio of red/green fluorescence, (f) Cell viability in the absence or presence of Fer-1, (e) Expression of ferritin and GPX4 proteins.

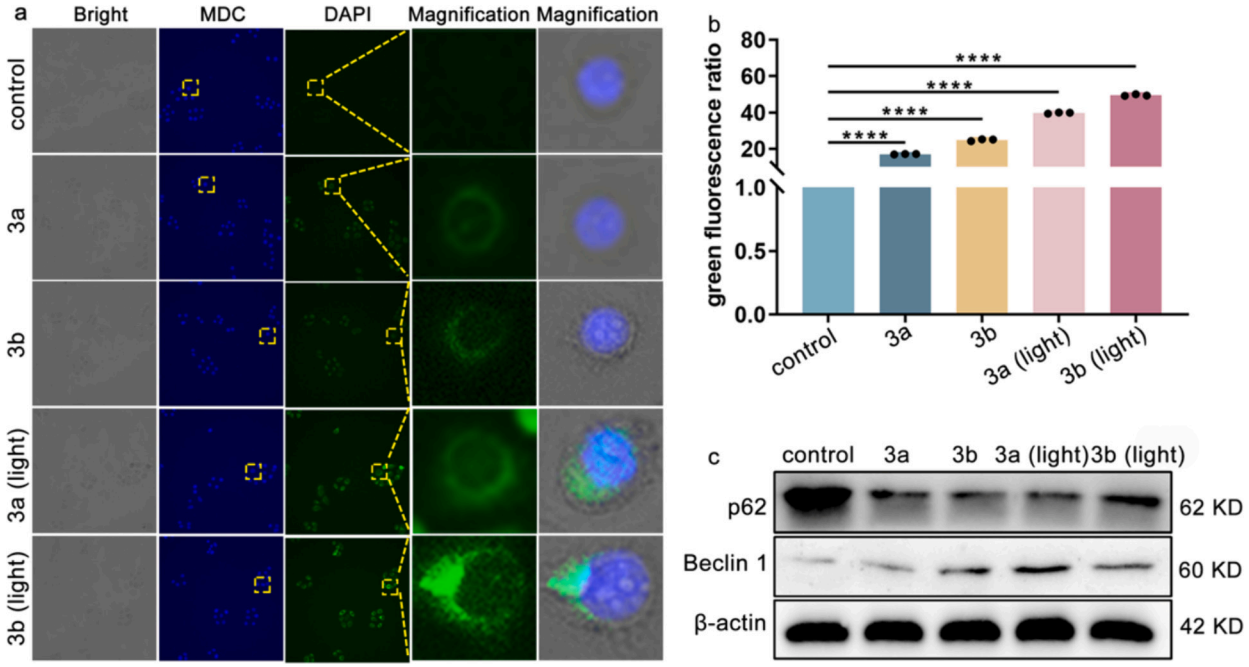

Fig. 7. (a) Assay of autophagy with MDC staining, (b) green fluorescence intensity, (c) expression of Beclin-1 and p62 after an exposure of A549 cells to IC_{50} concentration of 3a, 3b, 3a (light) and 3b (light) for 26 h. (For interpretation of the references to colour in this figure legend, the reader is referred to the web version of this article.)

further support that complexes are ability to initiate autophagy.

3.11. Photoactivation of the complexes induces immunogenic cell death (ICD)

Immunogenic cell demise (ICD) is a controlled manner in the cellular demise that has the potential to trigger an adaptive immune response in a robust immunological setting. It falls under the category of an unspecified phenomenon caused by particular chemotherapy medications, oncolytic viruses, physical chemotherapy, photodynamic therapy, and radiation therapy [78,79]. Releasing molecules during cellular distress or demise can serve as immune system stimulants or indicators of potential harm. These indicators are commonly referred to as damage-associated molecular patterns (DAMPs) [80]. DAMPs encompass the presentation of calreticulin (CRT) and heat-shock proteins (HSP70) on the surface of cells, extracellular release of adenosine triphosphate (ATP), high-mobility group box-1 (HMGB1), type I IFNs, and members belonging to the interleukin-1 (IL-1) cytokine family [81]. To explore

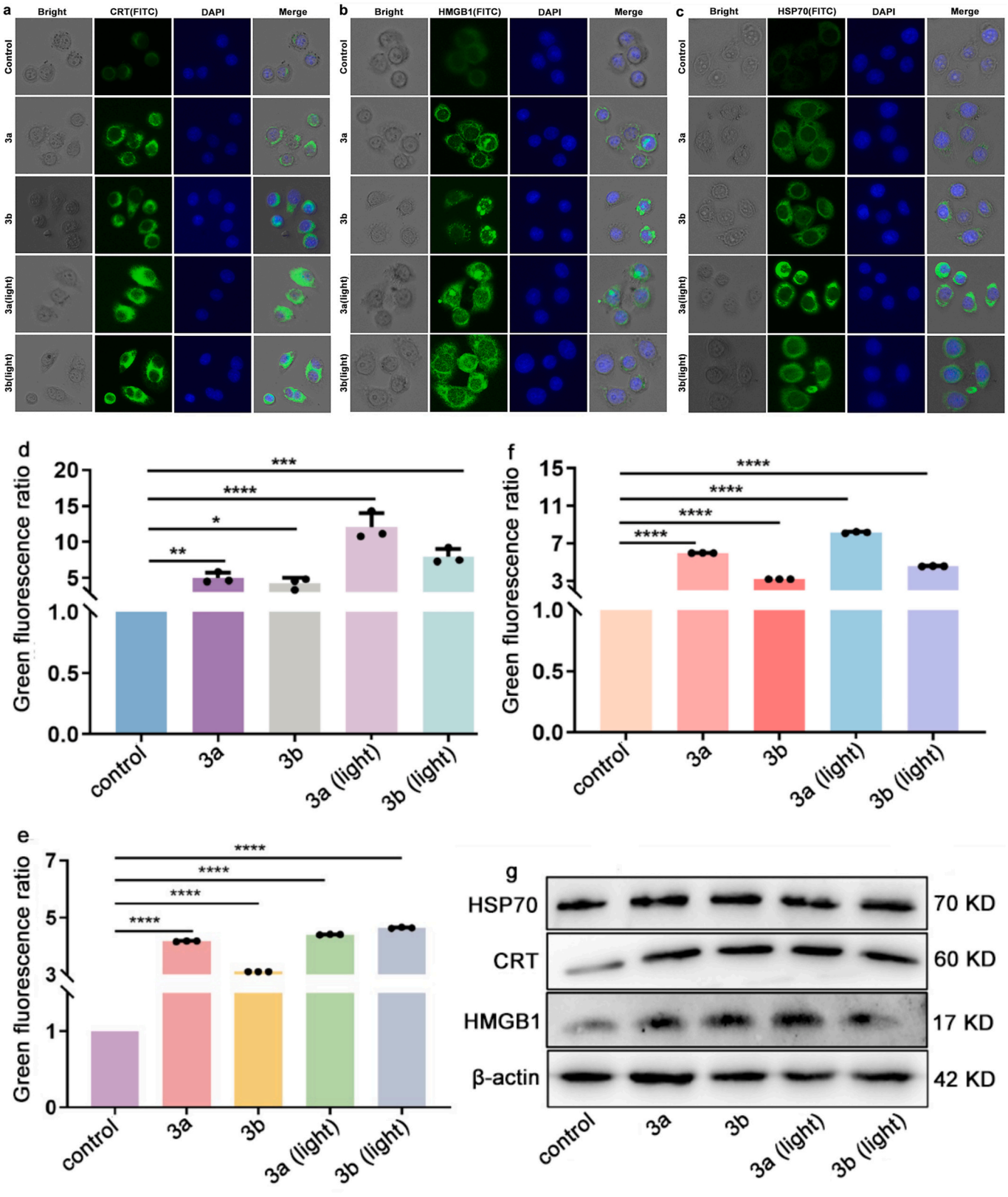

Fig. 8. ICD assay of CRT (a), HMGB1 (b) and HSP70 (c), the green fluorescence intensity for CRT (d), HMGB1 (e) and HSP70 (f) (***$p < 0.001$), (g) expression of proteins CRT, HMGB1 and HSP70. (For interpretation of the references to colour in this figure legend, the reader is referred to the web version of this article.)

the relationship between the complexes and ICD, we utilized immunofluorescence staining to detect changes in CRT, HMGB1, and HSP70 content. As depicted in Fig. 8a-c, treatment of A549 cells with 3a, 3b, 3a (light), 3b (light), green fluorescence increases, indicating 3a, 3b, 3a (light), 3b (light) can enhance CRT, HMGB1, and HSP70 content. The quantitative determination of green fluorescence intensity (3a, 3b as reference) further confirmed that complexes led to an increase of intracellular CRT, HSP70 and HMGB1 content (Fig. 8d-f).

Next, we assessed the impact of the complexes on the expression levels of CRT, HSP90, and HMGB1. As depicted in Fig. 8g, we discovered a significant increase in the expression levels of CRT, HSP70, and HMGB1. This further substantiates that the complexes may induce immunogenic cell demise.

The luminometer was utilized to measure the content of ATP. As presented in **Fig. S17** (SI), the ATP content was determined to be 2.56 μM in the control. 3a, 3b, 3a (light) and 3b (light) induce an increase of 2.00, 1.13, 3.33 and 2.50 μM in ATP content, respectively. These findings suggest that exposure of cells to the complexes significantly elevates ATP levels in A549 cells, leading to immunogenic cell death.

4. Conclusions

We successfully designed and synthesized complexes 3a, 3b and 3c. The pK_a values of 3a-3c are >4, indicating an ability of 3a-3c to enter the cell. The results from cytotoxicity experiments hint that 3a and 3b show better cytotoxic activity on A549 cells upon irradiation, The cytotoxicity of the complexes is closely related to the single state oxygen and quantum yields. The cellular uptake showed that 3a and 3b could enter the cell and accumulate in the cytoplasm. The wound healing, colony-forming and cell cycle experiments validate that both 3a and 3b could significantly inhibit the migration and proliferation in the S phase. 3a and 3b were found to increase lipid oxidation, downregulated the expression of Ferritin and GPX4, further cause ferroptosis. MDC staining indicated that the complexes could induce autophagy which was further supported by the changes related to indicators such as p62 and Beclin-1 expression. Immunofluorescence staining results revealed that complexes 3a and 3b interact on the mitochondria, facilitate MPTP opening, leading to a decrease of mitochondrial membrane potential, and release of cytochrome *c*, further activating caspase 3, regulating the expression of Bcl-2 family proteins, ultimately resulting in apoptosis. Additionally, 3a and 3b increase CRT, HMGB1, and HSP70 expression, thus promote immunogenic cell death (ICD). Taken together, we conclude that 3a and 3b cause cell death through autophagy, apoptosis, immunogenic cell death and ferroptosis. This work is valuable for developing effective PDT as potent anticancer drugs.

Author statement

We state that the manuscript has been finished by all authors listed in the manuscript. The all data are original and real. We agree to be accountable for all aspects of the work to ensure that questions related to the accuracy or integrity of any part of the work are appropriately investigated and resolved.

All authors have read the manuscript and approved the manuscript to be submitted to JIB.

CRediT authorship contribution statement

Gechang Li: Writing – original draft, Methodology, Investigation. **Jing Chen:** Methodology, Investigation. **Yufeng Xie:** Software, Data curation. **Yan Yang:** Writing – review & editing, Methodology. **Yajie Niu:** Formal analysis. **Xiaolan Chen:** Software, Formal analysis. **Xiandong Zeng:** Methodology. **Lin Zhou:** Methodology, Data curation. **Yunjun Liu:** Supervision, Project administration, Conceptualization.

Declaration of competing interest

The authors declare no competing interest exists.

Data availability

Data will be made available on request.

Acknowledgements

We are grateful for National Natural Science Foundation of China (No 21877018).

Appendix A. Supplementary data

Supplementary data to this article can be found online at https://doi.org/10.1016/j.jinorgbio.2024.112652.

References

[1] K.A. Robb, A.E. Simon, A. Miles, J. Wardle, Public perceptions of cancer: a qualitative study of the balance of positive and negative beliefs, BMJ Open 4 (2014) e005434.
[2] P.S. Roy, B.J. Saikia, Cancer and cure: a critical analysis, Indian J. Cancer 53 (2016) 441–442.
[3] C.M. Tilsed, S.A. Fisher, A.K. Nowak, R.A. Lake, W.J. Lesterhuis, Cancer chemotherapy: insights into cellular and tumor microenvironmental mechanisms of action, Front. Oncol. 12 (2022) 960317.
[4] E. Jakobsen, K.E. Olsen, M. Bliddal, M. Hornbak, G.F. Persson, A. Green, Forecasting lung cancer incidence, mortality, and prevalence to year 2030, BMC Cancer 21 (2021) 985.
[5] N.P.E. Barry, P.J. Sadler, Exploration of the medical periodic table: towards new targets, Chem. Commun. 49 (2013) 5106–5131.
[6] Z.D. Bugari, J. Bogojeski, B. Petrovi, S. Hochreuther, R.V. Eldik, Mechanistic studies on the reactions of platinum(II) complexes with nitrogen- and sulfur-donor biomolecules, Dalton Trans. 41 (2012) 12329–12345.
[7] D. Wang, S.J. Lippard, D. Wang, S.J. Lippard, Cellular processing of platinum anticancer drugs, Nat. Rev. Drug Discov. 4 (2005) 307–320.
[8] P. Agostinis, K. Berg, K.A. Cengel, T.H. Foster, A.W. Girotti, S.O. Gollnick, S. M. Hahn, M.R. Hamblin, A. Juzeniene, D. Kessel, M. Korbelik, J. Moan, P. Mroz, D. Nowis, J. Piette, B.C. Wilson, J. Golab, Photodynamic therapy of cancer: an update, J. Clin. 61 (2011) 250–281.
[9] Z. Liu, A. Habtemariam, A.M. Pizarro, S.A. Fletcher, A. Kisova, O. Vrana, L. Salassa, P.C. Bruijnincx, G.J. Clarkson, V. Brabec, P.J. Sadler, Organometallic half-sandwich iridium anticancer complexes, J. Med. Chem. 54 (2011) 3011–3026.
[10] W.J. Wang, Y.Y. Ling, Y.M. Zhong, Z.Y. Li, C.P. Tan, Z.W. Mao, Ferroptosis-enhanced cancer immunity by a ferrocene-appended iridium(III) diphosphine complex, Angew. Chem. Int. Ed. 61 (2022) e202115247.
[11] F.L. Xie, Z.T. Huang, L. Bai, J.W. Zhu, H.H. Xu, Q.Q. Long, Q.F. Guo, Y. Wu, S. H. Liu, Antitumor activity studies of iridium (III) polypyridine complexes-loaded liposomes against gastric tumor cell in vitro, J. Inorg. Biochem. 225 (2021) 111603.
[12] Y.Y. Ling, W.J. Wang, L. Hao, X.W. Wu, J.H. Liang, H. Zhang, Z.W. Mao, C.P. Tan, Self-amplifying iridium(III) photosensitizer for ferroptosis-mediated immunotherapy against transferrin receptor-overexpressing cancer, Small 18 (2022) e2203659.
[13] R. Guan, Y. Chen, L. Zeng, T.W. Rees, C. Jin, J. Huang, Z.S. Chen, L. Ji, H. Chao, Oncosis-inducing cyclometalated iridium(III) complexes, Chem. Sci. 9 (2018) 5183–5190.
[14] J. Weynand, A. Moreno-Betancourt, F. Loiseau, N. Berthet, E. Defrancq, B. Elias, Redox-active bis-cyclometalated iridium(III) complex as a DNA photo-cleaving agent, Inorg. Chem. 59 (2020) 2426–2433.
[15] B. Liu, X. Huang, M. Hu, Z. Chen, W. Zhang, Y. Li, Mitochondria-targeted cyclometalated iridium (III) complex for H_2S-responsive intracellular redox regulation as potent photo-oxidation anticancer agent, J. Biol. Inorg. Chem. 27 (2022) 641–651.
[16] S.O. Aderinto, T. John, A. Onawole, R.P. Galleh, J.A. Thomas, Iridium(III)-based minor groove binding complexes as DNA photocleavage agents, Dalton Trans. 53 (2024) 7282–7291.
[17] J. Chen, H. Liu, Y. Chen, H. Hu, C. Huang, Y. Wang, L. Liang, Y. Liu, Iridium(III) complexes inhibit the proliferation and migration of BEL-7402 cells through the PI3K/AKT/mTOR signaling pathway, J. Inorg. Biochem. 241 (2023) 112145.
[18] Y. Chen, Y. Gu, H. Hu, H. Liu, W. Li, C. Huang, J. Chen, L. Liang, Y. Liu, Design, synthesis and biological evaluation of liposome entrapped iridium(III) complexes toward SGC-7901 cells, J. Inorg. Biochem. 241 (2023) 112134.
[19] L. Liang, Y. Yang, H. Liu, F. Yuan, Y. Yuan, W. Li, C. Huang, J. Chen, Y. Liu, Synthesis, characterization, anticancer efficacy evaluation of ruthenium(II) and iridium(III) polypyridyl complexes toward A549 cells, J. Biol. Inorg. Chem. 28 (2023) 421–437.

[20] C. Huang, Y. Yuan, G. Li, S. Tian, H. Hu, J. Chen, L. Liang, Y. Wang, Y. Liu, Mitochondria-targeted iridium(III) complexes encapsulated in liposome induce cell death through ferroptosis and gasdermin-mediated pyroptosis, Eur. J. Med. Chem. 265 (2024) 116112.
[21] J. Chen, W. Li, G. Li, X. Liu, C. Huang, H. Nie, L. Liang, Y. Wang, Y. Liu, Targeted liposomes encapsulated iridium(III) compound greatly enhance anticancer efficacy and induce cell death via ferroptosis on HepG2 cells, Eur. J. Med. Chem. 265 (2024) 116078.
[22] W.Y. Zhang, Q.Y. Yi, Y.J. Wang, F. Du, M. He, B. Tang, D. Wan, Y.J. Liu, H. L. Huang, Photoinduced anticancer activity studies of iridium(III) complexes targeting mitochondria and tubules, Eur. J. Med. Chem. 151 (2018) 568–584.
[23] W. Li, C. Shi, X. Wu, Y. Zhang, H. Liu, X. Wang, C. Huang, L. Liang, Y. Liu, Light activation of iridium(III) complexes driving ROS production and DNA damage enhances anticancer activity in A549 cells, J. Inorg. Biochem. 236 (2022) 111977.
[24] L.F. Tan, H. Chao, DNA-binding and photocleavage studies of mixed polypyridyl ruthenium(II) complexes with calf thymus DNA, Inorg. Chim. Acta 360 (2007) 2016–2022.
[25] S. Sprouse, K.A. King, P.J. Spellane, R.J. Watts, Photophysical effects of metal-carbon bonds in ortho-metalated complexes of Ir(III) and Rh(III), J. Am. Chem. Soc. 106 (1984) 6647–6653.
[26] T. Mosmann, Rapid colorimetric assay for cellular growth and survival: application to proliferation and cytotoxicity assays, J. Immunol. Methods 65 (1983) 55–63.
[27] D.T. Manallack, The pK(a) distribution of drugs: application to drug discovery, Perspect. Med. Chem. 1 (2007) 25–38.
[28] E. Baka, J.E.A. Comer, K. Takács-Novák, Study of equilibrium solubility measurement by saturation shake-flask method using hydrochlorothiazide as model compound, J. Pharm. Biomed. Anal. 46 (2008) 335–341.
[29] L.V. Lutkus, S.S. Rickenbach, T.M. Mccormick, Singlet oxygen quantum yields determined by oxygen consumption, J. Photochem. Photobiol. A 378 (2019) 131–135.
[30] K. Bhattacharyya, P.K. Das, Quantitative aspects of all-trans-retinol singlet and. Triplet quenching by oxygen, Chem. Phys. Lett. 116 (1985) 326–331.
[31] M.J. Frisch, G.W. Trucks, H.B. Schlegel, G.E. Scuseria, M.A. Robb, J.R. Cheeseman, G. Scalmani, V. Barone, B. Mennucci, G.A. Petersson, H. Nakatsuji, M. Caricato, X. Li, H.P. Hratchian, A.F. Izmaylov, J. Bloino, G. Zheng, J.L. Sonnenberg, M. Hada, M. Ehara, K. Toyota, R. Fukuda, J. Hasegawa, M. Ishida, T. Nakajima, Y. Honda, O. Kitao, H. Nakai, T. Vreven, J.A. Montgomery Jr., J.E. Peralta, F. Ogliaro, M. Bearpark, J.J. Heyd, E. Brothers, K.N. Kudin, V.N. Staroverov, T. Keith, R. Kobayashi, J. Normand, K. Raghavachari, A. Rendell, J.C. Burant, S.S. Iyengar, J. Tomasi, M. Cossi, N. Rega, J.M. Millam, M. Klene, J.E. Knox, J.B. Cross, V. Bakken, C. Adamo, J. Jaramillo, R. Gomperts, R.E. Stratmann, O. Yazyev, A. J. Austin, R. Cammi, C. Pomelli, J.W. Ochterski, R.L. Martin, K. Morokuma, V. G. Zakrzewski, G.A. Voth, P. Salvador, J.J. Dannenberg, S. Dapprich, A.D. Daniels, O. Farkas, J.B. Foresman, J.V. Ortiz, J. Cioslowski, D.J. Fox, Gaussian 09, Revision D.01, Gaussian, Inc., Wallingford CT, 2013.
[32] S. Tian, Q.Y. Nie, H.M. Chen, L.J. Liang, H.Y. Hu, S.H. Tang, J.W. Yang, Y.J. Liu, H. Yin, Synthesis, characterization and irradiation enhances anticancer activity of liposome-loaded iridium(III) complexes, J. Inorg. Biochem. 256 (2024) 112549.
[33] X.C. Liu, Z.H. Wang, X.R. Zhang, X.C. Lv, Y. Song, R.X. Dong, G.X. Li, X.Y. Ren, Z. Y. Ji, X.A. Yuan, Z. Liu, Configurationally regulated half-sandwich iridium(III)-ferrocene heteronuclear metal complexes: potential anticancer agents, J. Inorg. Biochem. 249 (2023) 112393.
[34] I.M. Adjei, B. Sharma, V. Labhasetwar, Nanoparticles: cellular uptake and cytotoxicity, Adv. Exp. Med. Biol. 811 (2014) 73–91.
[35] G. Zhang, Z. Gao, X. Guo, R. Ma, X. Wang, P. Zhou, C. Li, Z. Tang, R. Zhao, P. Gao, CAP2 promotes gastric cancer metastasis by mediating the interaction between tumor cells and tumor-associated macrophages, J. Clin. Invest. 133 (2023) e166224.
[36] D. Liao, Y. Liu, C. Li, B. He, G. Zhou, Y. Cui, H. Huang, Arctigenin hinders the invasion and metastasis of cervical cancer cells via the FAK/paxillin pathway, Heliyon 9 (2023) e16683.
[37] F.J. Sulzmaier, C. Jean, D.D. Schlaepfer, FAK in cancer: mechanistic findings and clinical applications, Nat. Rev. Cancer 14 (2014) 598–610.
[38] J.A. Kellum, L.S. Chawla, Cell-cycle arrest and acute kidney injury: the light and the dark sides, nephrology, dialysis, transplantation, Nephrol. Dial. Transplant. 31 (2016) 16–22.
[39] S.J. Baker, E.P. Reddy, CDK4: a key player in the cell cycle, development, and cancer, Genes Cancer 3 (2012) 658–669.
[40] S.W. Taylor, E. Fahy, B. Zhang, G.M. Glenn, D.E. Warnock, S. Wiley, A.N. Murphy, S.P. Gaucher, R.A. Capaldi, B.W. Gibson, S.S. Ghosh, Characterization of the human heart mitochondrial proteome, Nat. Biotechnol. 21 (2003) 281–286.
[41] J. Liu, Y. Wu, G. Yang, Z. Liu, X. Liu, Mitochondrial targeting half-sandwich iridium(III) and ruthenium(II) dppf complexes and in vitro anticancer assay, I. Inorg. Biochem. 239 (2023) 112069.
[42] J. Adler, I. Parmryd, Quantifying colocalization by correlation: the Pearson correlation coefficient is superior to the Mander's overlap coefficient, Cytom. Part A 77A (2010) 733–742.
[43] S.B. Berman, T.G. Hastings, Dopamine oxidation alters mitochondrial respiration and induces permeability transition in brain mitochondria: implications for Parkinson's disease, J. Neurochem. 73 (1999) 1127–1137.
[44] S. Hussain, Measurement of nanoparticle-induced mitochondrial membrane potential alterations, Methods Mol. Biol. 2019 (1894) 123–131.
[45] X. Liu, C.N. Kim, J. Yang, R. Jemmerson, X. Wang, Induction of apoptotic program in cell-free extracts: requirement for dATP and cytochrome c, Cell 86 (1996) 147–157.
[46] H.J. Lee, H.J. Lee, E.O. Lee, S.G. Ko, H.S. Bae, C.H. Kim, K.S. Ahn, J. Lu, S.H. Kim, Mitochondria-cytochrome C-caspase-9 cascade mediates isorhamnetin-induced apoptosis, Cancer Lett. 270 (2008) 342–353.
[47] R.M. Mohammad, I. Muqbil, L. Lowe, C. Yedjou, H.Y. Hsu, L.T. Lin, M.D. Siegelin, C. Fimognari, N.B. Kumar, Q.P. Dou, H. Yang, A.K. Samadi, G.L. Russo, C. Spagnuolo, S.K. Ray, M. Chakrabarti, J.D. Morre, H.M. Coley, K. Honoki, H. Fujii, A.G. Georgakilas, A. Amedei, E. Niccolai, A. Amin, S.S. Ashraf, W. G. Helferich, X. Yang, C.S. Boosani, G. Guha, D. Bhakta, M.R. Ciriolo, K. Aquilano, S. Chen, S.I. Mohammed, W.N. Keith, A. Bilsland, D. Halicka, S. Nowsheen, A. S. Azmi, Broad targeting of resistance to apoptosis in cancer, Semin. Cancer Biol. 35 (2015) S78–S103.
[48] R.S. Wong, Apoptosis in cancer: from pathogenesis to treatment, J. Exp. Clin. Cancer Res. 30 (2011) 87.
[49] D. King, D. Yeomanson, H.E. Bryant, PI3King the lock: targeting the PI3K/Akt/mTOR pathway as a novel therapeutic strategy in neuroblastoma, J. Pediatr. Hematol. Oncol. 37 (2015) 245–251.
[50] S.M. Johnson, P. Gulhati, B.A. Rampy, Y. Han, P.G. Rychahou, H.Q. Doan, H. L. Weiss, B.M. Evers, Novel expression patterns of PI3K/Akt/mTOR signaling pathway components in colorectal cancer, J. Am. Coll. Surg. 210 (2010) 767–776.
[51] O. Cohausz, F.R. Althaus, Role of PARP-1 and PARP-2 in the expression of apoptosis-regulating genes in HeLa cells, J. Am. Coll. Surg. 25 (2009) 379–391.
[52] Z.Q. Wang, L. Stingl, C. Morrison, M. Jantsch, M. Los, K. Schulze-Osthoff, E. F. Wagner, PARP is important for genomic stability but dispensable in apoptosis, Genes Dev. 11 (1997) 2347–2358.
[53] E. Eskandari, C.J. Eaves, Paradoxical roles of caspase-3 in regulating cell survival, proliferation, and tumorigenesis, J. Cell Biol. 221 (2022) e202201159.
[54] A. Gross, J.M. Mcdonnell, S.J. Korsmeyer, BCL-2 family members and the mitochondria in apoptosis, Genes Dev. 13 (1999) 1899–1911.
[55] H.Y. Yong, M.S. Koh, A. Moon, The p38 MAPK inhibitors for the treatment of inflammatory diseases and cancer, Expert Opin. Investig. Drugs 18 (2009) 1893–1905.
[56] S.M. Eswarappa, P.L. Fox, Antiangiogenic VEGF-ax: a new participant in tumor angiogenesis, Cancer Res. 75 (2015) 2765–2769.
[57] H. Pu, Q. Zhang, C. Zhao, L. Shi, Y. Wang, J. Wang, M. Zhang, VEGFA involves in the use of fluvastatin and zoledronate against breast cancer, Pathol. Oncol. Res. 24 (2018) 557–565.
[58] S.J. Dixon, K.M. Lemberg, M.R. Lamprecht, R. Skouta, E.M. Zaitsev, C.E. Gleason, D.N. Patel, A.J. Bauer, A.M. Cantley, W.S. Yang, B. Morrison 3rd, B.R. Stockwell, Ferroptosis: an iron-dependent form of nonapoptotic cell death, Cell 149 (2012) 1060–1072.
[59] S.J. Dixon, B.R. Stockwell, The role of iron and reactive oxygen species in cell death, Nat. Chem. Biol. 10 (2014) 9–17.
[60] Y. Xu, Y. Li, J. Li, W. Chen, Ethyl carbamate triggers ferroptosis in liver through inhibiting GSH synthesis and suppressing Nrf2 activation, Redox Biol. 53 (2022) 102349.
[61] A.K. Holley, D.K. St Clair, Watching the watcher: regulation of p53 by mitochondria, Future Oncol. 5 (2009) 117–130.
[62] Z. Feng, W. Hu, E. de Stanchina, A.K. Teresky, S. Jin, S. Lowe, A.J. Levine, The regulation of AMPK beta1, TSC2, and PTEN expression by p53: stress, cell and tissue specificity, and the role of these gene products in modulating the IGF-1-AKT-mTOR pathways, Cancer Res. 67 (2007) 3043–3053.
[63] A. Saleem, H.N. Carter, D.A. Hood, p53 is necessary for the adaptive changes in cellular milieu subsequent to an acute bout of endurance exercise, Am. J. Phys. Cell Physiol. 306 (2014) C241–C249.
[64] W.S. Yang, R. SriRamaratnam, M.E. Welsch, K. Shimada, R. Skouta, V. S. Viswanathan, J.H. Cheah, P.A. Clemons, A.F. Shamji, C.B. Clish, L.M. Brown, A. W. Girotti, V.W. Cornish, S.L. Schreiber, B.R. Stockwell, Regulation of ferroptotic cancer cell death by GPX4, Cell 156 (2014) 317–331.
[65] Z. Xiao, B. Kong, J. Fang, T. Qin, C. Dai, W. Shuai, H. Huang, Ferrostatin-1 alleviates lipopolysaccharide-induced cardiac dysfunction, Bioengineered 12 (2021) 9367–9376.
[66] Q. Shi, R. Liu, L. Chen, Ferroptosis inhibitor ferrostatin-1 alleviates homocysteine-induced ovarian granulosa cell injury by regulating TET activity and DNA methylation, Mol. Med. Rep. 25 (2022) 130.
[67] P.F. Liu, Y.T. Feng, H.W. Li, X. Chen, G.S. Wang, S.Y. Xu, Y.L. Li, L. Zhao, Ferrostatin-1 alleviates lipopolysaccharide-induced lung injury via inhibiting ferroptosis, Cell. Mol. Biol. Lett. 25 (2020) 10.
[68] M. Plays, S. Müller, R. Rodriguez, Chemistry and biology of ferritin, Metallomics 13 (2021) mfab021.
[69] X. Fang, Z. Cai, H. Wang, D. Han, Q. Cheng, P. Zhang, F. Gao, Y. Yu, Z. Song, Q. Wu, P. An, S. Huang, J. Pan, H.Z. Chen, J. Chen, A. Linkermann, J. Min, F. Wang, Loss of cardiac ferritin H facilitates cardiomyopathy via Slc7a11-mediated ferroptosis, Circ. Res. 127 (2020) 486–501.
[70] K. Wang, Autophagy and apoptosis in liver injury, Cell Cycle 14 (2015) 1631–1642.
[71] J.D. Rabinowitz, E. White, Autophagy and metabolism, Science 330 (2010) 1344–1348.
[72] J.J. Wu, C. Quijano, J. Wang, T. Finkel, Metabolism meets autophagy, Cell Cycle 9 (2010) 4780–4781.
[73] W. Hou, Y. Xie, X. Song, X. Sun, M.T. Lotze, H.J. Zeh 3rd, R. Kang, D. Tang, Autophagy promotes ferroptosis by degradation of ferritin, Autophagy 12 (2016) 1425–1428.
[74] R. Kang, H.J. Zeh, M.T. Lotze, D. Tang, The Beclin 1 network regulates autophagy and apoptosis, Cell Death Differ. 18 (2011) 571–580.
[75] S.F. Funderburk, Q.J. Wang, Z. Yue, The Beclin 1-VPS34 complex at the crossroads of autophagy and beyond, Trends Cell Biol. 20 (2010) 355–362.

[76] X. Li, K.B. Yang, W. Chen, J. Mai, X.Q. Wu, T. Sun, R.Y. Wu, L. Jiao, D.D. Li, J. Ji, H.L. Zhang, Y. Yu, Y.H. Chen, G.K. Feng, R. Deng, J.D. Li, X.F. Zhu, CUL3 (cullin 3)-mediated ubiquitination and degradation of BECN1 (beclin 1) inhibit autophagy and promote tumor progression, Autophagy 17 (2021) 4323–4340.
[77] S.J. Jeong, X. Zhang, A. Rodriguez-Velez, T.D. Evans, B. Razani, p62/SQSTM1 and selective autophagy in cardiometabolic diseases, Antioxid. Redox Signal. 31 (2019) 458–471.
[78] L. Galluzzi, I. Vitale, S.A. Aaronson, J.M. Abrams, G. Kroemer, Molecular mechanisms of cell death: recommendations of the nomenclature committee on cell death 2018, Cell Death Differ. (2018) 486–541.
[79] A.D. Garg, L. Galluzzi, L. Apetoh, T. Baert, R.B. Birge, J.M. Bravo-San Pedro, K. Breckpot, D. Brough, R. Chaurio, M. Cirone, A. Coosemans, P.G. Coulie, D. D. Ruysscher, L. Dini, P.D. Witte, A.M. Dudek-Peric, A. Faggioni, J. Fucikova, U. S. Gaipl, J. Golab, M.L. Gougeon, M.R. Hamblin, A. Hemminki, M. Herrmann, J. W. Hodge, O. Kepp, G. Kroemer, D.V. Krysko, W.G. Land, F. Madeo, A.A. Manfredi, S.R. Mattarollo, C. Maueroder, N. Merendino, G. Multhoff, T. Pabst, J.E. Ricci, Chiara Riganti, Erminia Romano, Nicole Rufo, Mark J. Smyth, R. Jürgen Sonnemann, J. Spisek, E. Stagg, P. Vacchelli, L. Vandenabeele, B.J. Vandenberk, S. V. Van den Eynde, F. Gool, L. Velotti, P. Agostinis Zitvogel, Molecular and translational classifications of DAMPs in immunogenic cell death, Front. Immunol. 6 (2015) 588.
[80] D.V. Krysko, A.D. Garg, A. Kaczmarek, O. Krysko, P. Agostinis, P. Vandenabeele, Immunogenic cell death and DAMPs in cancer therapy, Nat. Rev. Cancer 12 (2012) 860–875.
[81] A. Ahmed, S.W.G. Tait, Targeting immunogenic cell death in cancer, Mol. Oncol. 14 (2020) 2994–3006.